Available online at www.sciencedirect.com
ScienceDirect
Physica D 237 (2008) 1507–1529
PHYSICA D
www.elsevier.com/locate/physd

Ghost manifolds in slow–fast systems, with applications to unsteady fluid flow separation

Amit Surana, George Haller*

Department of Mechanical Engineering, Massachusetts Institute of Technology, 77 Massachusetts Ave., Cambridge, MA 02139, USA

Available online 28 March 2008

Abstract

Consider a structurally stable nonhyperbolic critical manifold in a nonautonomous dynamical system. Despite the lack of hyperbolicity and slow dynamics, sharp moving spikes can develop and move along this critical manifold. An important physical example of this phenomenon is moving separation behind a cylinder in accelerating crossflow.

Using a combination of analytic and numerical methods, we uncover the geometric structure responsible for moving spikes. This structure, a *ghost manifold*, turns out to have a footprint on the critical manifold even though the two manifolds are separated by a boundary layer. We illustrate our results on analytical and numerical examples of off-wall fluid flow separation.

Keywords: Non-hyperbolic; Averaging; Wavelets; Flow separation

1. Introduction

Spike formation is a well-known phenomenon in molecular dynamics (e.g. classical water molecule [3]), neural science (e.g., Hodgkin–Huxley model [12]), optics (e.g., nonlinear Schrödinger equation [19]) and rigid body dynamics (see [9] for various examples). In these examples, spikes form because of the presence of two different time scales: slow evolution along an invariant manifold, and fast instability transverse to the manifold. At the heart of spike formation are unstable manifolds emanating from linearly unstable (hyperbolic) slow manifolds. The location of these spikes is fixed and can be determined from an analysis of the dynamics on the slow manifold [13]. The intensity of the spike is related to the hyperbolicity of the underlying slow manifold, and hence can be determined from linear analysis.

Some dynamical systems, however, exhibit spikes that defy the above paradigm. Specifically, there are non-autonomous systems that exhibit spikes moving along nonhyperbolic critical manifolds (manifolds of fixed points). Both the above-mentioned slow component on the manifold and the hyperbolic component transverse to the manifold are absent, yet robust spikes form and move in these problems.

An important physical example is moving unsteady separation along a no-slip wall of a fluid flow. This phenomenon can be observed experimentally by simply placing a cylinder in a two-dimensional crossflow of increasing speed [23]. The no-slip boundary of the cylinder is a nonhyperbolic critical manifold that is robust with respect to all physical perturbations. There is neither any slow boundary dynamics nor any linear instability along the cylinder surface, yet two material spikes emanate from the cylinder and move towards the wake as the Reynolds number increases (see Fig. 1). Since unstable manifolds emanating from points of a critical manifold cannot move along the critical manifold, this physical example exhibits dynamical behavior that cannot be explained by classical invariant manifold- and singular perturbation arguments. One faces a similar puzzle in trying to interpret smoke experiments that show moving separation points along accelerating airfoils.

* Corresponding author. Tel.: +1 617 4523064; fax: +1 617 2588742.
E-mail address: ghaller@mit.edu (G. Haller).

0167-2789/$ - see front matter
doi:10.1016/j.physd.2008.03.032

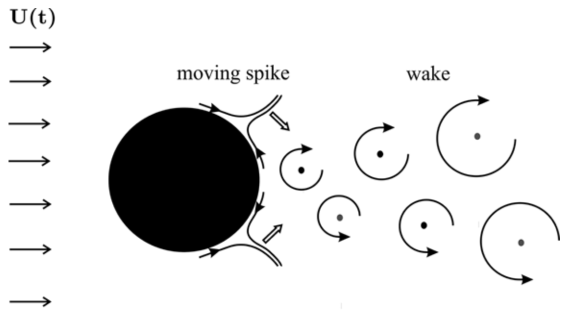

Fig. 1. Wake behind a stationary cylinder in a two dimensional time varying crossflow. Also shown are material spikes that move towards the wake as the Reynolds number increases.

Here we show that the moving spikes in the above examples are due to the presence of *ghost manifolds*, i.e., nonhyperbolic unstable manifolds that emanate from a boundary layer near the critical manifold. The boundary layer is thin, hence the misleading perception that unstable manifolds slide on critical manifolds. Still, these ghost manifolds turn out to have a virtual footprint on the critical manifold that can be detected, and hence the location of spike formation can be predicted from local analysis on the critical manifold. As far as we know, this paper is the first to describe and solve this problem mathematically.

We summarize these findings in a numerically assisted analytic criterion for moving spikes that we derive using a combination of rescaling, dynamic averaging, topological invariant techniques and wavelet analysis. Our moving spike criterion translates to a criterion for moving unsteady separation when applied to flow around aerodynamic bodies. We illustrate the use of this criterion in analytical and numerical examples of flow separation.

2. Motivation

Consider a dynamical system of the form

$$\dot{\mathbf{x}} = \mathbf{v}(\mathbf{x}, \epsilon t, t), \tag{1}$$

where $\mathbf{x} = (x, y) \in U \subset \mathbb{R}^2$, $\mathbf{v} = (u, v)$, and $\epsilon \ll 1$ is a nonnegative small parameter. System (1) is therefore a non-autonomous system whose time dependence has two components, one is of $\mathcal{O}(1)$ and one is of $\mathcal{O}(\epsilon)$ speed.

Assume that system (1) admits a smooth compact two-dimensional manifold $\mathcal{B}$ of fixed points that is independent of time. As an example, one can think of an unsteady fluid flow in which particle motions satisfy Eq. (1) with $\mathbf{v}$ denoting the velocity field of the fluid. In this case, any fixed no-slip boundary of the fluid is a time-independent critical manifold. By the form of (1), the fluid flow has a slowly evolving mean component as well as faster fluctuations.

Let $\mathbf{x}_b(s) = (x_b(s), y_b(s))$ be the arclength parametrization of $\mathcal{B}$ with s denoting the arclength that varies on a compact set I. The unit tangent and the outer unit normal to $\mathcal{B}$ will be denoted by $\mathbf{t}(s)$ and $\mathbf{n}(s)$, respectively. Then along $\mathcal{B}$, we have

$$\mathbf{v}(\mathbf{x}_b(s), \epsilon t, t) = 0, \qquad \mathbf{n}^{\mathrm{T}}(s)\nabla_{\mathbf{x}}\mathbf{v}(\mathbf{x}_b(s), \epsilon t, t)\mathbf{n}(s) = 0, \tag{2}$$

for all s and t. The second condition in (2) implies that the stretching rate normal to $\mathcal{B}$ vanishes identically along $\mathcal{B}$, which holds true for any flow that is locally incompressible along the critical manifold $\mathcal{B}$.

In order to separate the two time scales in the system (1) more explicitly, we introduce the phase variable

$$\phi = \epsilon t,$$

so that in extended phase space of the $(\mathbf{x}, \phi)$ variables, system (1) becomes

$$\begin{aligned} \dot{\mathbf{x}} &= \mathbf{v}(\mathbf{x}, \phi, t), \\ \dot{\phi} &= \epsilon. \end{aligned} \tag{3}$$

In the extended phase space, $\mathcal{B}$ shows up as an invariant slow manifold

$$\mathcal{S} = \{(\mathbf{x}_b(s), \phi) \mid s \in I, \phi \in \mathbb{R}\}, \tag{4}$$

with no motion in the $\mathbf{x}$-direction. and uniform slow motion in the ϕ-direction.

To focus on the dynamics near $\mathcal{S}$, we let

$$\mathbf{x}(s, \eta) = \mathbf{x}_b(s) + \eta\mathbf{n}(s),$$

where η is the distance from $\mathcal{S}$ along the normal $\mathbf{n}(s)$. After this transformation, system (3) can be written as

$$\begin{aligned}\dot{s} &= \tilde{u}(s, \eta, \phi, t),\\ \dot{\eta} &= \tilde{v}(s, \eta, \phi, t),\\ \dot{\phi} &= \epsilon,\end{aligned} \tag{5}$$

where

$$\begin{aligned}\tilde{u}(s, \eta, \phi, t) &= \frac{\mathbf{v}\left(\mathbf{x}_b(s) + \eta\mathbf{n}(s), \phi, t\right) \cdot \mathbf{t}(s)}{1 - \eta\kappa(s)},\\ \tilde{v}(s, \eta, \phi, t) &= \mathbf{v}\left(\mathbf{x}_b(s) + \eta\mathbf{n}(s), \phi, t\right) \cdot \mathbf{n}(s),\end{aligned} \tag{6}$$

with $\kappa(s) = x_b'(s)y_b''(s) - y_b'(s)x_b''(s)$ denoting the curvature of $\mathcal{B}$.

In the new coordinates (s, η, ϕ), the slow manifold $\mathcal{S}$ is simply given by $\eta = 0$, and the conditions (2) are equivalent to

$$\tilde{u}(s, 0, \phi, t) = 0, \qquad \tilde{v}(s, 0, \phi, t) = 0, \qquad \partial_\eta \tilde{v}(s, 0, \phi, t) = 0.$$

Because of these conditions, we can rewrite $(\tilde{u}, \tilde{v})$ as

$$\begin{aligned}\tilde{u}(s, \eta, \phi, t) &= \eta \int_0^1 \partial_\eta \tilde{u}(s, \eta p, \phi, t)\, \mathrm{d}p,\\ \tilde{v}(s, \eta, \phi, t) &= \eta^2 \int_0^1 \int_0^1 \partial_\eta^2 \tilde{v}(s, \eta pq, \phi, t) p\, \mathrm{d}p\mathrm{d}q.\end{aligned}$$

We introduce an additional blow-up of the normal coordinate near $\mathcal{S}$ by letting

$$\eta = \epsilon\tilde{\eta},$$

where $\epsilon \geq 0$ is a small parameter. Expanding in powers of ϵ and $\tilde{\eta}$, we obtain the dynamical system (5) in the form

$$\begin{aligned}\dot{s} &= \epsilon\tilde{\eta}\partial_\eta\tilde{u}(s, 0, \phi, t) + \epsilon^2\tilde{\eta}^2\left[\frac{1}{2}\partial_\eta^2\tilde{u}(s, 0, \phi, t) + \mathcal{O}(\tilde{\eta}\epsilon)\right],\\ \dot{\tilde{\eta}} &= \epsilon\tilde{\eta}^2\frac{1}{2}\partial_\eta^2\tilde{v}(s, 0, \phi, t) + \epsilon^2\tilde{\eta}^3\left[\frac{1}{6}\partial_\eta^2\tilde{v}(s, 0, \phi, t) + \mathcal{O}(\tilde{\eta}\epsilon)\right],\\ \dot{\phi} &= \epsilon,\end{aligned} \tag{7}$$

which can be thought of as a normal form of the original system (1) near $\mathcal{S}$ in the extended phase space.

3. Set-up and assumptions

Motivated by the normal formal (7), we now consider systems of the general form

$$\begin{aligned}\dot{\mathbf{x}} &= \epsilon\mathbf{f}(\mathbf{x}, \phi, t) + \epsilon^2\mathbf{g}(\mathbf{x}, \phi, t; \epsilon),\\ \dot{\phi} &= \Delta\epsilon,\end{aligned} \tag{8}$$

where $\mathbf{x} = (x, z)$, $\epsilon \geq 0$ is a small parameter, and $\Delta \in [0, 1]$ is a constant that we shall ultimately set to one to obtain results relevant for the normal form (7) and hence for our original system (1).

The functions

$$\mathbf{f}(\mathbf{x}, \phi, t) = \begin{pmatrix} zf_1(x, \phi, t)\\ z^2 f_2(x, \phi, t)\end{pmatrix}, \qquad \mathbf{g}(\mathbf{x}, \phi, t; \epsilon) = \begin{pmatrix} z^2[g_1(x, \phi, t) + \mathcal{O}(z\epsilon)]\\ z^3[g_2(x, \phi, t) + \mathcal{O}(z\epsilon)]\end{pmatrix}, \tag{9}$$

and their derivatives are assumed to be uniformly bounded in time in a neighborhood of the invariant nonhyperbolic slow manifold

$$\mathcal{S} = \{(\mathbf{x},\phi) : x \in I,\ z = 0, \phi \in \mathbb{R}\}.$$

We note that $z = \frac{y}{\epsilon}$ denotes a rescaled coordinate normal to $\mathcal{S}$.

In this general setting, we further assume the function $\mathbf{f}(\mathbf{x}, \phi, t)$ can be decomposed into a slowly evolving mean and fluctuations as follows:

$$\mathbf{f}(\mathbf{x}, \phi, t) = \mathbf{f}^0(\mathbf{x}, \phi) + \tilde{\mathbf{f}}(\mathbf{x}, \phi, t), \tag{10}$$

where

$$\lim_{T\to\infty} \frac{1}{T} \int_{t_0}^{t_0-T} \tilde{\mathbf{f}}(\mathbf{x}, \phi, \tau)\, \mathrm{d}\tau = 0,$$
$$\limsup_{T\to\in f t y} \left| \int_{t_0}^{t_0-T} \tilde{\mathbf{f}}(\mathbf{x}, \phi, \tau)\, \mathrm{d}\tau \right| < \infty,$$
$$\limsup_{T\to\infty} \left| \int_{t_0}^{t_0-T} \nabla_{\mathbf{x}}\tilde{\mathbf{f}}(\mathbf{x}, \phi, \tau)\, \mathrm{d}\tau \right| < \infty, \tag{11}$$

for any t_0. The fluctuating part $\tilde{\mathbf{f}}$ can be time-periodic or irregular in time. The lack of dependence of $\mathbf{f}^0$ explicitly on t creates a frequency gap between the mean and fluctuations, as is typical in turbulent fluid flows [18].

4. Ghost manifold

4.1. Invariant manifolds in the $\Delta = 0$ limit

We now rewrite the decomposition (10) of system (8) as

$$\dot{\mathbf{x}} = \epsilon[\mathbf{f}^0(\mathbf{x}, \phi) + \tilde{\mathbf{f}}(\mathbf{x}, \phi, t)] + \epsilon^2 \mathbf{g}(\mathbf{x}, \phi, t; \epsilon),$$
$$\dot{\phi} = \epsilon\Delta. \tag{12}$$

Therefore, up to $\mathcal{O}(\epsilon)$, the mean dynamics near the slow manifold $\mathcal{S}$ is governed by the system

$$\dot{\mathbf{x}} = \epsilon\mathbf{f}^0(\mathbf{x}, \phi),$$
$$\dot{\phi} = \epsilon\Delta. \tag{13}$$

Taking the $\Delta = 0$ limit, we obtain the equivalent system

$$\dot{x} = z f_1^0(x, z, \phi),$$
$$\dot{z} = z^2 f_2^0(x, z, \phi),$$
$$\dot{\phi} = 0. \tag{14}$$

Observe that the manifold $\mathcal{S} = \{(x, z, \phi) \mid z = 0\}$ is a critical manifold (manifold of fixed points) for system (14). Localized pulse formation can be observed in system (14) along any smooth curve $\mathcal{C} \subset \mathcal{S}$ of the form

$$\mathcal{C} = \{(p(\phi), 0, \phi) : \phi \in \mathcal{I} \subset \mathbb{R}\}, \tag{15}$$

provided that

$$f_1^0(p(\phi), \phi) = 0$$
$$\sup_{\phi\in\mathcal{I}} \partial_x f_1^0(p(\phi), \phi) < 0,$$
$$\inf_{\phi\in\mathcal{I}} f_2^0(p(\phi), \phi) > 0. \tag{16}$$

Indeed, if we rescale time via $\frac{\mathrm{d}\tau}{\mathrm{d}t} = \epsilon z(t)$ along trajectories of system (14), then conditions (16) render the set $\mathcal{C}$ a hyperbolic curve of fixed points with a two-dimensional unstable manifold $\mathcal{W}_0$ off the $\mathcal{S}$ plane, and with a two-dimensional stable manifold within the $\mathcal{S}$ plane. In forward time, $\mathcal{W}_0$ attracts nearby trajectories in the vicinity of $\mathcal{C}$, and forces them to eject from a neighborhood of $\mathcal{S}$. Passing back to the original time t, we therefore obtain a nonhyperbolic unstable manifold $\mathcal{W}_0$ emanating from the critical manifold $\mathcal{S}$ along the curve $\mathcal{C}$ (see Fig. 2).

For $\Delta > 0$, manifolds $\mathcal{C}$ and $\mathcal{W}_0$ no longer remain invariant for system (13), in which the slow manifold $\mathcal{S}$ is now filled with ($x =$ const., $z = 0$) invariant lines. Because of uniform drift on these lines in the ϕ direction, there cannot be any other invariant set within $\mathcal{S}$ that is C^1-close $\mathcal{C}$ (unless $\mathcal{C}$ is itself a straight line).

Therefore, $\mathcal{C}$ typically has no smooth continuation for $\Delta > 0$. Still, numerical simulations indicate that trajectories of system (8) will continue to be ejected from the vicinity $\mathcal{S}$ (see Fig. 4), forming spikes that appear to be moving along $\mathcal{C}$ as the phase variable ϕ (and hence time) increases. As we show below, this behavior is caused by a locally invariant piece $\mathcal{W}_\epsilon^g$ of the unstable manifold $\mathcal{W}_0$ that survives even for $\Delta = 1$ in system (8), as illustrated in Fig. 3. (By local invariance of a manifold we mean that trajectories can only leave the manifold through its boundary.)

The invariant manifold $\mathcal{W}_\epsilon^g$ lies off the slow manifold $\mathcal{S}$ and cannot be continued down to $\mathcal{S}$. We can therefore think of $\mathcal{W}_\epsilon^g$ as a locally invariant sheet that hovers over $\mathcal{S}$. For this reason, we shall refer to $\mathcal{W}_\epsilon^g$ as a *ghost manifold*.

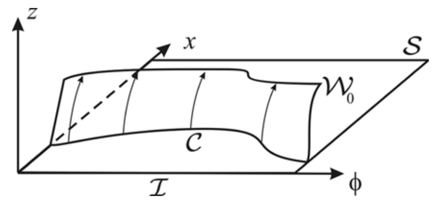

Fig. 2. The geometry of the manifolds $\mathcal{S}$, $\mathcal{C}$ and $\mathcal{W}_0$ for $\Delta = 0$ under conditions (16).

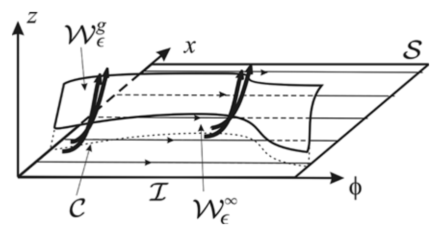

Fig. 3. The geometry of the ghost manifold $\mathcal{W}_\epsilon^g$ for $\Delta > 0$. $\mathcal{W}_\epsilon^g$ is the locally invariant piece of $\mathcal{W}_\epsilon^\infty$, which is the counterpart of $\mathcal{W}_0$ that survies the perturbation $\Delta = 1$ in the modified system Eq. (17), as described in Section 4.2.

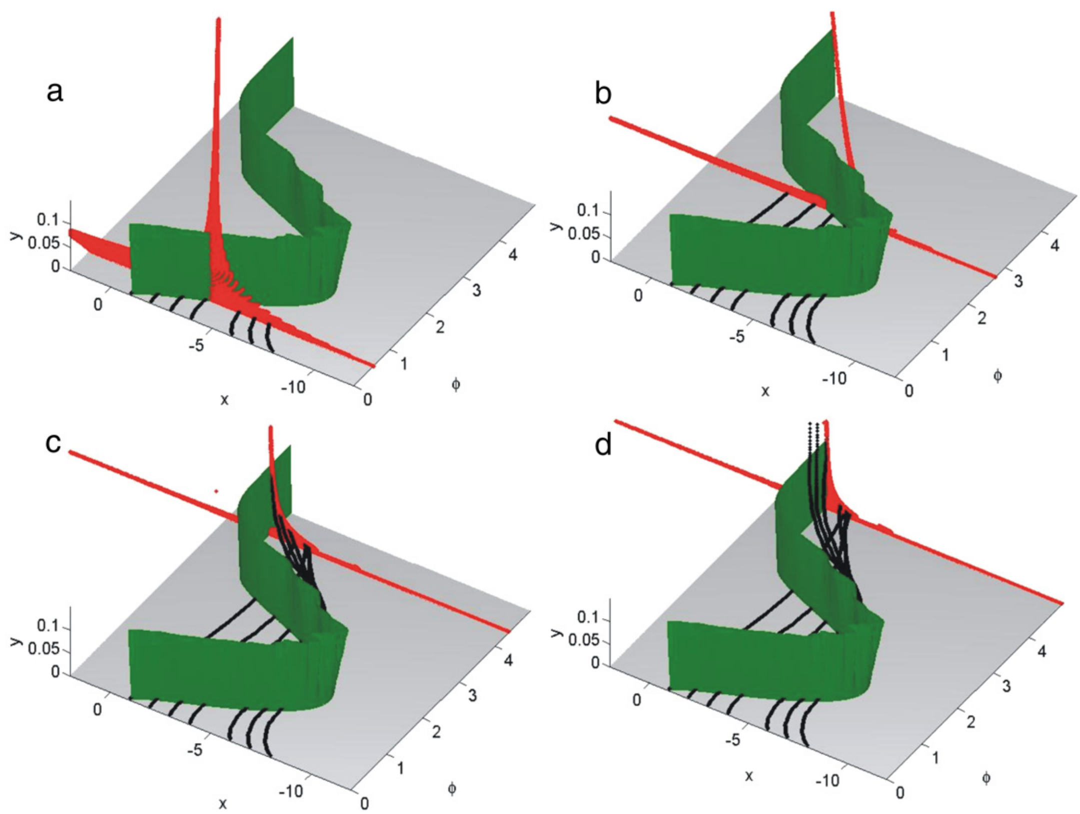

Fig. 4. Separation geometry in the extended phase space (x, y, ϕ) associated with the separation bubble flow for the case $G(\phi) = a\sin(\phi t)$ and $H(\phi, t) = [c + d\sin(\epsilon t)]\, r(t)$ with $a = 2$, $c = 2$, $d = 0$, $\epsilon = 0.1$, $\beta = 4$. The subplots (a)–(d) correspond to the time instants $t = 5.50$, $t = 22.00$, $t = 38.50$, and $t = 44.00$.

4.2. Existence of a ghost manifold

In order to prove the existence of a ghost manifold $\mathcal{W}_\epsilon^g$ discussed above, we consider the modified version of system (12) of the form

$$\begin{aligned} \dot{\mathbf{x}} &= \epsilon[\mathbf{f}^0(\mathbf{x}, \phi) + \tilde{\mathbf{f}}(\mathbf{x}, \phi, t)] + \epsilon^2 \mathbf{g}(\mathbf{x}, \phi, t; \epsilon), \\ \dot{\phi} &= \epsilon \Delta M(z), \end{aligned} \tag{17}$$

where $M(z)$ is a C^∞ bump function (see, e.g., [1]) satisfying

$$M(z)\begin{cases} = 0 & z \le \frac{1}{q}z^* \\ \in (0,1) & \frac{1}{q}z^* < z < z^* \\ = 1 & z \ge z^*. \end{cases} \tag{18}$$

The parameter $z^* > 0$ and $q > 1$ will be chosen later, see Appendix C for details.

Note that the inclusion of the bump function in (17) makes no difference for $z \ge z^*$, but freezes the dynamics in the ϕ direction close to the slow manifold $\mathcal{S}$. As a result, $\mathcal{C}$ continues to be an invariant manifold for system (17) even for $\Delta > 0$. We shall construct an unstable manifold for $\mathcal{C}$ in the modified system (17) for $\Delta = 1$. We shall then argue that a subset of this unstable manifold will play the role of the ghost manifold $\mathcal{W}_\epsilon^g$ discussed above.

Applying averaging (see Appendix A), topological invariant manifold techniques as described in Appendix B and scaling analysis, we prove in Appendix C that under appropriate conditions, $\mathcal{W}_0$ perturbs into a nearby unstable manifold $\mathcal{W}_\epsilon^g$ for $\mathcal{C}$ in the modified system (17). Specifically, we have the following result:

Theorem 1. *Assume that there exists $\epsilon_0 > 0$ such that the conditions*

$$\begin{aligned} & f_1^0(p(\phi),\phi) = 0 \\ & \sup_{\phi\in\mathcal{I}} \partial_x f_1^0(p(\phi),\phi) < 0, \\ & \inf_{\phi\in\mathcal{I}} f_2^0(p(\phi),\phi) > 0, \\ & \inf_{\phi\in\mathcal{I}} \left[f_2^0(p(\phi),\phi) - \partial_x f_1^0(p(\phi),\phi) - \epsilon\left|p'(\phi)\right| \right] > 0, \end{aligned} \tag{19}$$

are satisfied for all $\phi \in \mathcal{I} = (-\infty, \epsilon t_0)$. Then, for all $\epsilon < \epsilon_0$ small enough and for $z^* = \frac{1}{\sqrt{\epsilon}}$, $q \approx 1$ and $\Delta = 1$, the modified system (17) admits an unstable manifold $\tilde{\mathcal{W}}_\epsilon^\infty$ emanating from the curve $\mathcal{C}$.

The term $f_2^0(x,\phi) - \partial_x f_1^0(x,\phi)$ measures the rate of stretching normal to the slow manifold $\mathcal{S}$. The term $|p'(\phi)|$ is the speed at which $p(\phi)$ varies in the slow time scale. The fourth condition in (19) therefore requires that the rate of normal stretching along $p(\phi)$ should be larger than the speed of the leading-order spike location $p(\phi)$.

Since system (17) coincides with (12) for $z \ge z^*$, we obtain that a locally invariant subset of $\mathcal{W}_\epsilon^\infty$ also exists in system (12) in the form

$$\mathcal{W}_\epsilon^g = \mathcal{W}_\epsilon^\infty \bigcap \{(x,y,t) \mid y \ge y^*,\ t \le t_0\}, \tag{20}$$

in the extended phase space (x, y, t) for the original system (3), where

$$y^* = \epsilon z^* = \sqrt{\epsilon}$$

and $\mathcal{W}_\epsilon^\infty$ is the rescaled version of $\tilde{\mathcal{W}}_\epsilon^\infty$.

The locally invariant manifold $\mathcal{W}_\epsilon^g$ is the ghost manifold we sketched in Fig. 3. Its existence is guaranteed as long as conditions (19) hold on all available velocity data up to a present time t_0. If only finite-time velocity information is available up to t_0, the present construction of $\mathcal{W}_\epsilon^g$ can be combined with the finite-time invariant manifold approach used in [10].

As we show in Appendix D, second-order averaging can be used to obtain an approximation for the slope of $\mathcal{W}_\epsilon^\infty$ along $\mathcal{C}$. The resulting slope $s(\phi)$ of $\mathcal{W}_\epsilon^\infty$ relative to the normal $\mathbf{n}$ of $\mathcal{S}$ satisfies

$$s(\phi) = \frac{F^0(p(\phi),\phi)}{f_2^0(p(\phi),\phi) - \partial_x f_1^0(p(\phi),\phi)}, \tag{21}$$

for each $\phi \in \mathcal{I}$, where

$$F(x,\phi,t;t_0) = g_1(x,t) + f_1(x,\phi,t)\int_{t_0}^t [f_2(x,\phi,\tau) - f_2^0(x,\phi)]\mathrm{d}\tau + [\partial_x f_1(x,\phi,t) - f_2^0(x,\phi)]\int_{t_0}^t f_1(x,\phi,\tau)\mathrm{d}\tau. \tag{22}$$

Formula (21) can be used to approximate the slope of $\mathcal{W}_\epsilon^g$ as well for small enough ϵ.

4.3. Dynamic averaging using wavelets

The application of Theorem 1 in Section 4.2 requires the mean component $\mathbf{f}^0(\mathbf{x}, \epsilon t)$ of $\mathbf{f}(\mathbf{x}, \epsilon t, t)$ to be available. In applications, this time-varying mean component is not readily available and hence must be identified numerically. We denote the operation of extracting the mean of $\mathbf{f}(\mathbf{x}, \phi, t)$ by $\langle \cdot \rangle$, so that

$$\langle \mathbf{f} \rangle (\mathbf{x}, \phi) = \mathbf{f}^0(\mathbf{x}, \phi) = \langle \mathbf{f}(\mathbf{x}, \phi, t) \rangle . \tag{23}$$

Since we are concerned with extraction of the temporal mean, here we shall suppress the dependence of $\mathbf{f}$ on spatial variables.

The simplest approach to finding it would be finite-time averaging ([18]). In this approach, the mean operator is defined as

$$\langle f \rangle (\phi_0) = \frac{1}{2T_m(t_0)} \int_{t_0 - T_m(t_0)}^{t_0 + T_m(t_0)} f(\tau) \mathrm{d}\tau,$$

where $T_m(t_0)$ is an appropriate time scale depending on the current time t_0 and $\phi_0 = \epsilon t_0$. There is no obvious choice for the averaging interval $T_m(t_0)$: one typically argues that $T_m(t_0)$ should be large in comparison with characteristic period of the fluctuating quantity $\tilde{\mathbf{f}}$, but small in comparison with period of the evolving mean $\langle \mathbf{f} \rangle$ in the vicinity of current time t_0. The result of this type of mean extraction will strongly depend on the choice of $T_m(t_0)$.

More powerful mean extraction methods have been developed for the purpose of signal processing. From a signal processing perspective, extraction of the mean of $\mathbf{f}$ is just the classical problem of *denoising*. Denoising seeks to provide a good approximation for a signal from its noisy measurements. In our context, noise is the high-frequency oscillatory component $\tilde{\mathbf{f}}(\mathbf{x}, \phi, t)$ with the signal of interest being $\mathbf{f}^0(\mathbf{x}, \phi)$.

One of the basic approaches to denoising is the generalized Fourier series technique. In such an analysis, the underlying function is expanded into an orthogonal series with corresponding generalized Fourier coefficients estimated from noisy data. By shrinking or truncating these coefficients and taking an inverse Fourier transform, a smoothed approximation to the underlying function is obtained.

For non-local basis functions (such as trigonometric functions), however, shrinking Fourier coefficients will also affect the global shape of the reconstructed function and hence introduce unwanted artifacts. Therefore, classical Fourier-based techniques will have serious limitations for non-stationary and inhomogeneous signals [7] arising in applications such as turbulent fluid flows.

By contrast, wavelet-based smoothing methods provide a natural and flexible approach to the estimation of the true function from their noisy versions due to their ability to respond to local variations without allowing pathological behavior (see, e.g., [16,4,14]). We, therefore, propose wavelet-based denoising as an effective means to implement the averaging operator (23) numerically.

Giving a self-contained introduction to wavelets is beyond the scope of this paper; we refer the reader to [7] and the references cited therein for a description of wavelets for applications to fluid mechanics. In numerical examples considered in Section 6, we shall use Matlab's Wavelet Toolbox and its standard built-in denoising functions to carry out the averaging operation (23).

5. Fluid flow separation

5.1. Physical set-up

In this section we discuss the application of Theorem 1 to moving flow separation or flow attachment on a no-slip boundary of an unsteady fluid flow. Consider a two-dimensional time-dependent velocity field $\mathbf{v}(\mathbf{x}, t) = (u(\mathbf{x}, t), v(\mathbf{x}, t))$ describing a fluid flow on a two-dimensional spatial domain parameterized by the coordinates $\mathbf{x} = (x, y)$. Assume that $\mathbf{v}$ and its derivatives are uniformly bounded in the vicinity of a no-slip boundary at $y = 0$, on which $\mathbf{v}$ satisfies

$$\mathbf{v}(x, 0, t) \equiv 0$$

for all times. We also assume that the flow satisfies the continuity equation

$$\rho_t + \nabla \cdot (\rho \mathbf{v}) = 0, \tag{24}$$

where $\rho(\mathbf{x}, t)$ denotes the fluid density. More general curved boundaries can also be treated as described in Section 2.

Fluid flow separation is loosely defined as the detachment of fluid from the boundary. (Flow attachment is the opposite phenomenon that can be thought of as flow separation in backward time.) The detachment of fluid is characterized by the formation of a material spike that is readily observable in laboratory-and numerical experiments. Systematic studies of this spike formation date back to the seminal work of Prandtl [21] in 1904. He showed that two-dimensional *steady flows* ($\mathbf{v}$ has no explicit time dependence) separate from a no-slip boundary at points where the wall shear $\partial_y u(x, 0)$ vanishes and admits a negative gradient. Similarly, at points of steady attachment, $\partial_y u(x, 0)$ vanishes and admits a positive gradient.

An extension of Prandtl's criteria to fixed separation and attachment in unsteady two-dimensional flows was obtained recently by [11,15]. They used invariant manifold techniques to locate time-dependent material spikes emanating from fixed locations on the boundary. Their main result is simple to state for incompressible flows: material spike formation takes place up to the present time t_0 at a boundary point $\mathbf{p} = \left(x_p, 0\right)$ whenever

$$\lim_{T\to\infty} \frac{1}{T}\int_{t_0}^{t_0-T} u_y(\mathbf{p}, s)\,\mathrm{d}s = 0, \qquad \limsup_{T\to\infty} \frac{1}{T}\int_{t_0}^{t_0-T} u_{xy}(\mathbf{p}, s)\,\mathrm{d}s < 0. \tag{25}$$

The conditions for fixed attachment are similar, with the direction of the inequality reversed and lim sup changed to lim inf in the second condition.

Note that the separation point $\mathbf{p}$ in (25) is fixed in time, thus the criterion cannot capture a moving separation. As we described in the Introduction, however, there are important examples of flow separation that involve time-varying separation locations. In these examples, the flow admits periodic or turbulent temporal fluctuations that are superimposed on a slower evolutionary component of the velocity field. For instance, one may observe a moving separation location on the wing of a turning aircraft. The turning of the plane, however fast it may feel to the human observer, still takes place on time scales that are much longer than time scales of local turbulent fluctuations near the wing.

Moving material spikes in such flows cannot be generated by classical unstable manifolds, since any unstable manifold would necessarily be tied to fixed points on the boundary. We now discuss how ghost manifolds can be used to locate moving unsteady separation and attachment.

We start by assuming the presence of a slowly-varying mean component in the velocity field, which enable us to write the equation of particle motions as

$$\mathbf{x} \dot{=} v(\mathbf{x}, \epsilon t, t) = (u(\mathbf{x}, \epsilon t, t), v(\mathbf{x}, \epsilon t, t)), \tag{26}$$

where $0 < \epsilon \ll 1$. We introduce the change of variables

$$y = \epsilon z \mathrm{e}^{\int_{t_0}^{t} v_y(x,0,\epsilon\tau,\tau)\,\mathrm{d}\tau}, \tag{27}$$

which transforms the particle motion (26) to the form (8) (cf. Kilic et al. [15] for details) with

$$\mathbf{f}(\mathbf{x}, \epsilon t, t) = \begin{pmatrix} zA(x, 0, \epsilon t, t) \\ z^2 C(x, 0, \epsilon t, t) \end{pmatrix}, \qquad \mathbf{g}(\mathbf{x}, \epsilon t, t; \epsilon) = \begin{pmatrix} z^2[A_y(x, 0, \epsilon t, t) + \mathcal{O}(z\epsilon)] \\ z^3[C_y(x, 0, \epsilon t, t) + \mathcal{O}(z\epsilon)] \end{pmatrix}, \tag{28}$$

and

$$\begin{aligned} A(x, z, \epsilon t, t) &= \mathrm{e}^{\int_{t_0}^{t} v_y(x,0,\epsilon\tau,\tau)\mathrm{d}\tau} u_y(x, z\mathrm{e}^{\int_{t_0}^{t} v_y(x,0,\epsilon\tau,\tau)\mathrm{d}\tau}, \epsilon t, t), \\ C(x, z, \epsilon t, t) &= \frac{1}{2}\mathrm{e}^{\int_{t_0}^{t} v_y(x,0,\epsilon\tau,\tau)\mathrm{d}\tau} v_{yy}(x, 0, \epsilon t, t) + O(z). \end{aligned} \tag{29}$$

We note that the conservation of mass condition (24) is crucial in obtaining the locally incompressible normal form (28).

We assume that $\mathbf{f}$ admits a decomposition

$$\mathbf{f}(\mathbf{x}, \phi, t) = \langle \mathbf{f} \rangle (\mathbf{x}, \phi) + \tilde{\mathbf{f}}(\mathbf{x}, \phi, t),$$

in the vicinity of the $z = 0$ boundary, where we have used the operator notation introduced in Section 4.3. The fluctuating part of $\mathbf{f}$ is assumed to satisfy

$$\lim_{T\to\infty} \frac{1}{T}\int_{t_0}^{t_0-T} \tilde{\mathbf{f}}(\mathbf{x}, \phi, \tau)\,\mathrm{d}\tau = 0.$$

The above assumptions put us in the general framework considered in Section 4.2. In the present context, a moving point $\mathbf{p}\,(\epsilon t)$ satisfying conditions (16) marks locations of zero shear for the mean component of $\mathbf{v}$. This is therefore the location of separation one would obtain by applying Prandtl's steady condition to the mean component of an unsteady flow at each time instant. This is to be contrasted with the widespread practice in the separation literature to apply Prandtl's condition instantaneously to the full velocity field $\mathbf{v}$. We shall see in examples how the latter procedure fails to identify the location of material spike formation correctly.

Theorem 1 asserts that applying Prandtl's criterion to the mean flow is correct as long as the motion of the Prandtl point $\mathbf{p}\,(\epsilon t)$ obtained in this fashion is not too fast (cf. last condition in (19)). In that case, there exists a ghost manifold $\mathcal{W}_\epsilon^g$ near the Prandtl point, generating a spike that co-moves with $\mathbf{p}\,(\epsilon t)$ near the no-slip boundary $y = 0$. In the extended phase space of the (x, y, ϕ) variables, for each $\phi \in \mathcal{I}$, we let

$$\mathcal{W}_\epsilon^g(t) = \mathcal{W}_\epsilon^g \bigcap \{(x, y, \phi) \mid \phi = \epsilon t,\ t \in (-\infty, t_0)\}, \tag{30}$$

be the intersection of $\mathcal{W}_\epsilon^g$ with the $\phi =$ const. plane. In the physical space (x, y), $\mathcal{W}_\epsilon^g(t)$ is then an attracting material line that attracts and ejects particles from the vicinity of the $y = 0$ boundary without having a point of attachment to that boundary. $\mathcal{W}_\epsilon^g(t)$ is therefore the center of a moving spike that can be predicted from its on-wall signature $\mathbf{p}\,(\epsilon t)$.

5.2. Moving separation and attachment criteria

We are now spell out the moving separation and attachment criteria that are obtained by applying Theorem 1 to a mass-conserving time-dependent velocity field satisfying the assumptions of Section 5.1

Theorem 2. *Up to time t_0, moving separation due to a ghost manifold exists near the point $\mathbf{p}(\epsilon t) = (p(\epsilon t), 0)$ if for all $\phi \in \mathcal{I} = (-\infty, \epsilon t_0]$,*

$$\langle A\rangle (p(\phi), 0, \phi) = 0, \tag{31}$$

$$\sup_{\phi\in\mathcal{I}} \langle A_x\rangle (p(\phi), 0, \phi) < 0, \tag{32}$$

$$\inf_{\phi\in\mathcal{I}} \langle C\rangle (p(\phi), 0, \phi) > 0, \tag{33}$$

$$\inf_{\phi\in\mathcal{I}} \left[\langle C\rangle (p(\phi), 0, \phi) - \langle A_x\rangle (p(\phi), 0, \phi) - \epsilon|p'(\phi)|\right] > 0. \tag{34}$$

The last condition (34) in the above theorem is the only one that cannot be anticipated from an instantaneous application of Prandtl's steady result. This last condition states that for moving separation to occur near $\mathbf{p}(\epsilon t)$, particles should be ejected at a rate faster than the speed at which the separation point moves. A directly computable form of this condition can be obtained by differentiating (31) with respect to ϕ, which gives

$$p'(\phi) \langle A_x\rangle (p(\phi), 0, \phi) + \left\langle A_\phi\right\rangle (p(\phi), 0, \phi) = 0,$$

or, by (32),

$$p'(\phi) = -\frac{\left\langle A_\phi\right\rangle (p(\phi), 0, \phi)}{\langle A_x\rangle (p(\phi), 0, \phi)}.$$

This enables us to rewrite (34) as

$$\inf_{\phi\in\mathcal{I}} \left[\langle C\rangle (p(\phi), 0, \phi) - \langle A_x\rangle (p(\phi), 0, \phi) - \epsilon \left|\frac{\left\langle A_\phi\right\rangle (p(\phi), 0, \phi)}{\langle A_x\rangle (p(\phi), 0, \phi)}\right|\right] > 0.$$

From the formula (21), we conclude that the slope $s(t_0)$ of moving separation profile $\mathcal{W}_\epsilon^g(t_0)$ at t_0 is approximately given by

$$s(t_0) = \frac{\langle F\rangle (p(\epsilon t_0), 0, \epsilon t_0)}{\langle C\rangle (p(\epsilon t_0), 0, \epsilon t_0) - \langle A_x\rangle (p(\epsilon t_0), 0, \epsilon t_0)}, \tag{35}$$

where

$$\begin{aligned} F(\mathbf{x}, \phi, t; t_0) = {} & \frac{1}{2}\mathrm{e}^{2\int_{t_0}^{t} v_y(x,0,\phi,\tau)\mathrm{d}\tau} u_{yy}(\mathbf{x}, \phi, t) + A(\mathbf{x}, \phi, t) \int_{t_0}^{t} [C(\mathbf{x}, \phi, \tau) - \langle C\rangle (\mathbf{x}, \phi)]\mathrm{d}\tau \\ & + [A_x(\mathbf{x}, \phi, t) - \langle C\rangle (\mathbf{x}, \phi)] \int_{t_0}^{t} A(\mathbf{x}, \phi, \tau)\mathrm{d}\tau. \end{aligned} \tag{36}$$

Applying Theorem 1 in backward time, we obtain the following attachment criterion for moving attachment in unsteady flows satisfying the assumptions of Section 5.1.

Theorem 3. *Starting from time t_0, moving attachment due to a ghost manifold exists near the point $\mathbf{p}(\epsilon t) = (p(\epsilon t), 0)$ if for all $\phi \in \mathcal{I} = [\epsilon t_0, +\infty)$,*

$$\langle A\rangle (p(\phi), 0, \phi) = 0,$$

$$\inf_{\phi\in\mathcal{I}} \langle A_x\rangle (p(\phi), 0, \phi) > 0,$$

$$\sup_{\phi\in\mathcal{I}} \langle C\rangle (p(\phi), 0, \phi) < 0,$$

$$\sup_{\phi\in\mathcal{I}} \left[\langle C\rangle (p(\phi), 0, \phi) - \langle A_x\rangle (p(\phi), 0, \phi) - \epsilon \left|\frac{\left\langle A_\phi\right\rangle (p(\phi), 0, \phi)}{\langle A_x\rangle (p(\phi), 0, \phi)}\right|\right] < 0.$$

The slope of moving attachment profile relative to the normal of the wall again satisfies formula (21). Note that to identify moving attachment, Theorem 3 requires a knowledge of future velocity data, which is typically not available.

6. Examples

6.1. Separation bubble flow

In this section we revisit unsteady bubble flow studied previously in the context of fixed unsteady flow separation in [11] and [15]. The general incompressible velocity field for the bubble model is given by

$$u(x,y,t) = -y + 3y^2 + x^2y - \frac{2}{3}y^3 + \beta xyF(t),$$
$$v(x,y,t) = -xy^2 - \frac{1}{2}\beta y^2 F(t), \tag{37}$$

where $F(t)$ is any continuous function of time. Depending on the choice of $F(t)$, we can generate periodic, quasi-periodic or aperiodic time dependence for the velocity field.

In order to generate a flow with a time scale dichotomy, we take $F(t) = G(\phi) + H(\phi,t)$, where $H(\phi,t)$ satisfies

$$\lim_{T\to\infty} \frac{1}{T}\int_{t_0-T}^{t_0} H(\phi,t)\mathrm{d}t = 0.$$

For a numerical demonstration of our main results, we consider two cases:

$$G(\phi) = a\sin(\phi), \qquad G(\phi) = a\log(\phi + b).$$

In both cases, we select

$$H(t) = (c + d\sin(\phi))r(t),$$

where $r(t)$ is a zero mean random variable with a normal distribution and unit variance. Such a time dependence models a separation bubble with a well-defined slow mean growth, onto which substantial random oscillations are superimposed.

The velocity field (37) satisfies the hypothesis of Section 2 and can be decomposed as

$$\mathbf{v}(\mathbf{x},t) = \mathbf{v}^0(\mathbf{x},\phi) + \tilde{\mathbf{v}}(\mathbf{x},\phi,t),$$

with the components

$$\mathbf{v}^0(\mathbf{x},\phi) = \begin{pmatrix} -y + 3y^2 + x^2y - \frac{2}{3}y^3 + \beta xyG(\phi) \\ -xy^2 - \frac{1}{2}\beta y^2 G(\phi) \end{pmatrix}, \qquad \tilde{\mathbf{v}}(\mathbf{x},\phi,t) = H(\phi,t)\begin{pmatrix} \beta xy \\ -\frac{1}{2}\beta y^2 \end{pmatrix}. \tag{38}$$

With A defined in (29), the mean $\langle A\rangle$ can be identified analytically as

$$\langle A\rangle(x,0,\phi) = x^2 + \beta xG(\phi) - 1.$$

Hence, the only candidate for a moving separation point is (cf. (31)–(33))

$$p(\phi) = -\frac{\beta G(\phi)}{2} - \sqrt{\frac{(\beta G(\phi))^2}{4} + 1}, \tag{39}$$

where

$$\langle A_x\rangle(p(\phi),0,\phi) = -\langle C\rangle(p(\phi),0,\phi) = -\sqrt{(\beta G(\phi))^2 + 4} \le -2 < 0.$$

Furthermore, condition (34) takes the form

$$\langle C\rangle(p(\phi),0,\phi) - \langle A_x\rangle(p(\phi),0,\phi) - \epsilon\left|\frac{\langle A_\phi\rangle(p(\phi),0,\phi)}{\langle A_x\rangle(p(\phi),0,\phi)}\right| = 3\sqrt{\frac{(\beta G(\phi))^2}{4} + 1} - \epsilon\beta\left|\frac{G'(\phi)}{2} + \frac{\beta G(\phi)G'(\phi)}{\sqrt{\frac{(\beta G(\phi))^2}{4} + 1}}\right| > 0,$$

which is satisfied for the parameter values that we have chosen.

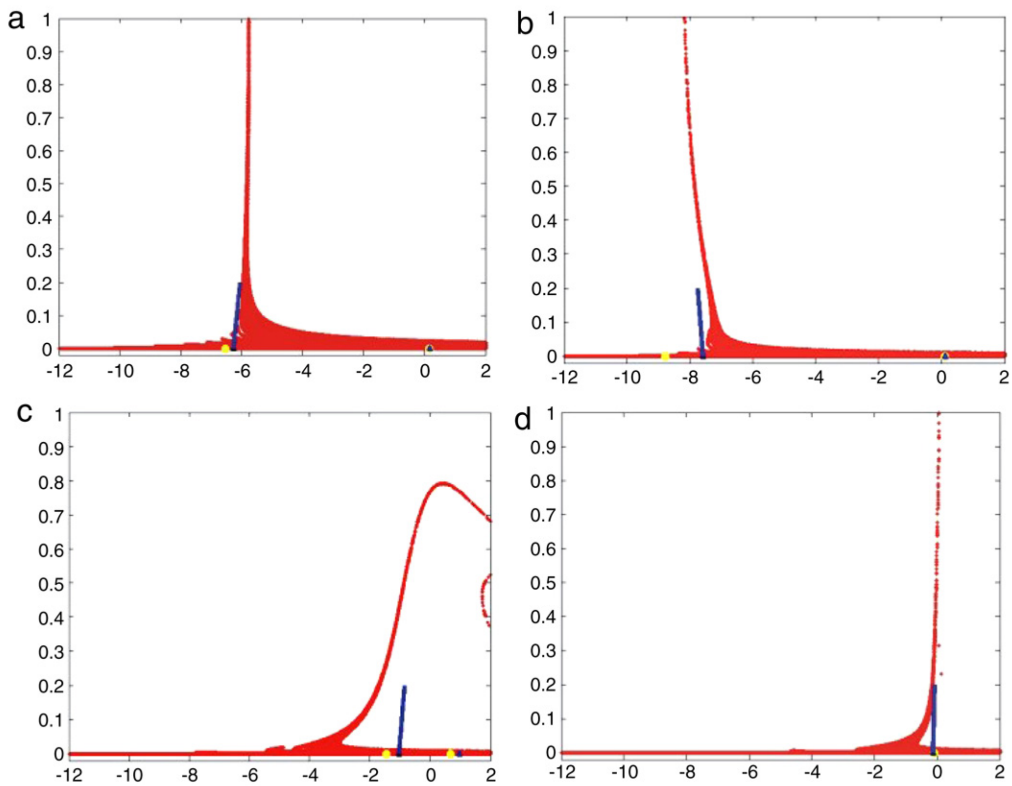

Fig. 5. Blue triangles show moving separation and reattachment locations obtained from Theorem 2, while yellow circles are the instantaneous wall-shear zeros. Also shown at the moving separation point is the linear approximation of the separation profile obtained from our slope formula. These snapshots clearly indicate that the particle spike tends to approach and align with the predicted separation profile. Subplots (a)–(d) correspond to times $t = 11.00$, $t = 21.80$, $t = 32.60$, and $t = 43.40$. Parameter values are the same as for the previous figure. (For interpretation of the references to colour in this figure legend, the reader is referred to the web version of this article.)

The slope formula (35) takes the concrete form

$$s(\phi) = \frac{\langle F \rangle (\phi)}{3\sqrt{((\beta G(\phi))^2 + 4)}}, \tag{40}$$

where

$$F(t, \phi; t_0) = 6 + 3\beta p(\phi)\,[2p(\phi) + \beta G(\phi)] \left[\int_{t_0}^{t} H(\phi, \tau)\mathrm{d}\tau + \beta^2 p(\phi) H(t) \int_{t_0}^{t} H(\phi, \tau)\mathrm{d}\tau \right],$$

One has to numerically extract the slowly evolving mean of $F(t, \phi; t_0)$ at t_0, regarding it as a function of t and ϕ.

We computed the separation location function $p(\phi)$ identified (39), and drew a line of slope (40) relative to the wall normal at each point of the curve $p(\phi)$. The resulting line bundle is the green surface in Fig. 4 that shows numerically simulated spike formation in the extended phase space of the (x, y, ϕ) variables. Also shown are some past (black) and many current (red) positions of fluid particles launched closed to the $y = 0$ no-slip wall.

We recall that the green surface is a visualization of $\mathcal{W}_\epsilon^\infty$, the unstable manifold of an auxiliary adiabatic system we used in the proof of Theorem 1. Therefore, only an off-wall portion of $\mathcal{W}_\epsilon^\infty$ will act as a ghost manifold that governs material spike formation. Indeed, it is evident from Fig. 4 that particles close to the boundary (shown in black) *intersect* $\mathcal{W}_\epsilon^\infty$ transversely, and hence $\mathcal{W}_\epsilon^\infty$ does not act as a locally invariant manifold in the immediate vicinity of the wall. Consequently, particles do not separate from the boundary along $\mathcal{W}_\epsilon^\infty$ but are attracted to the upper portion of $\mathcal{W}_\epsilon^\infty$. This upper portion is what we have referred to as the *ghost manifold* $\mathcal{W}_\epsilon^g$. The ghost manifold gives an accurate prediction for the location of the red spike, which changes as the slow phase variable $\phi = \epsilon t$ evolves in time.

Fig. 5 shows the particle paths in physical space (x, y) along with moving separation location and the linear approximation of the separation profile. Also shown in these plots as yellow circles are instantaneous wall-shear zeros, which are often considered as separation locations in the aerodynamics literature. As Fig. 5 shows, this practice is unjustified.

The second case we consider here is that of $G(\phi) = a\log(\phi + b)$, with $c \neq 0$ so that the $\tilde{\mathbf{v}}$ depends on the slow time scale as well. Snapshots of particle separation are shown in the Fig. 6. Again, the ghost manifold we compute correctly predicts the location and orientation of the spike.

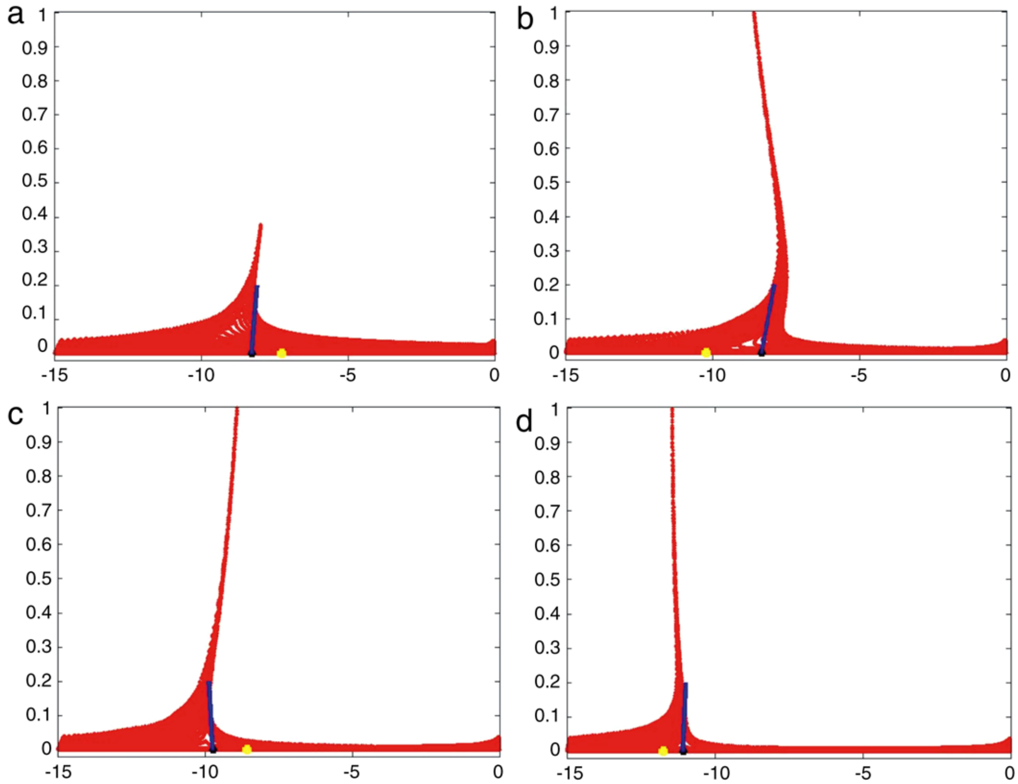

Fig. 6. Same as Fig. 5, but for the case $G(t) = a\log(\epsilon t + b)$ and $H(\phi, t) = [c + d\sin(\epsilon t)]r(t)$ with $a = 1.5$, $b = 3$, $c = 2.25$, $d = 1.5$, $\epsilon = 0.1$, $\beta = 4$. The subplots (a)–(d) correspond to the times $t = 3.60$, $t = 21.60$, $t = 27.00$, and $t = 37.80$.

6.2. Separation over a moving boundary

Steady flow patterns over a horizontally moving wall is a paradigm for moving separation. Indeed, if a spike forms at a fixed spatial location, that location becomes time-varying in a frame fixed to the wall. Sears and Tellionis [24] argued that a shear-layer develops in the vicinity of the wall that prevents one from predicting the separation location from wall-based observations.

In order to evaluate this argument, we consider an analytic model of a two-dimensional flow with a flat horizontal boundary that moves horizontally at speed U. Using the Perry–Chong procedure [22], we have derived a polynomial velocity field that is the solution of the Navier–Stokes equation up to fifth order in the distance from the moving wall. The velocity field is of the form

$$\begin{aligned} u(x,y,t) &= U + \alpha(t)y + y^2 + \beta(t)x^2y + \gamma(t)xy^2 - \frac{1}{3}\beta(t)y^3 + 15y^4 \\ &\quad - x^3y^2 + \frac{1}{2}\left[\frac{1}{6}\alpha(t)\beta(t) + 1\right]xy^4 + \frac{1}{30}\alpha(t)\gamma(t)y^5, \\ v(x,y,t) &= -xy^2\beta(t) - \frac{1}{3}\gamma(t)y^3 + x^2y^3 - \frac{1}{10}\left[\frac{1}{6}\alpha(t)\beta(t) + 1\right]y^5, \end{aligned} \tag{41}$$

with U denoting the speed of the moving boundary at $y = 0$, and with time-dependent parameters, $\alpha(t) < 0, \beta(t) > 0$ and $\gamma(t)$.

We first assume that streamline patterns of flow are constant, i.e., we fix parameters $\alpha(t) = \alpha_0 < 0, \beta(t) = \beta_0 > 0$ and $\gamma(t) = \gamma_0$ in time. We show the relevant steady streamline geometries for upstream moving ($U < 0$) and downstream moving ($U > 0$) walls in Fig. 7(a)–(c). Similar streamlines patterns were sketched by Sears and Tellionis [24], corresponding to upstream-slipping type and downstream-slipping separation. From these figures, it appears that particles separate from the boundary due to a saddle-type stagnation point in the interior of the flow, without any connection to on-wall flow quantities, as suggested by Sears and Tellionis.

In order to analyze separation in the framework developed in this paper, we need to have a fixed boundary. To achieve this, we pass to a frame co-moving with the boundary by making the change of variables

$$\tilde{x} = x - Ut.$$

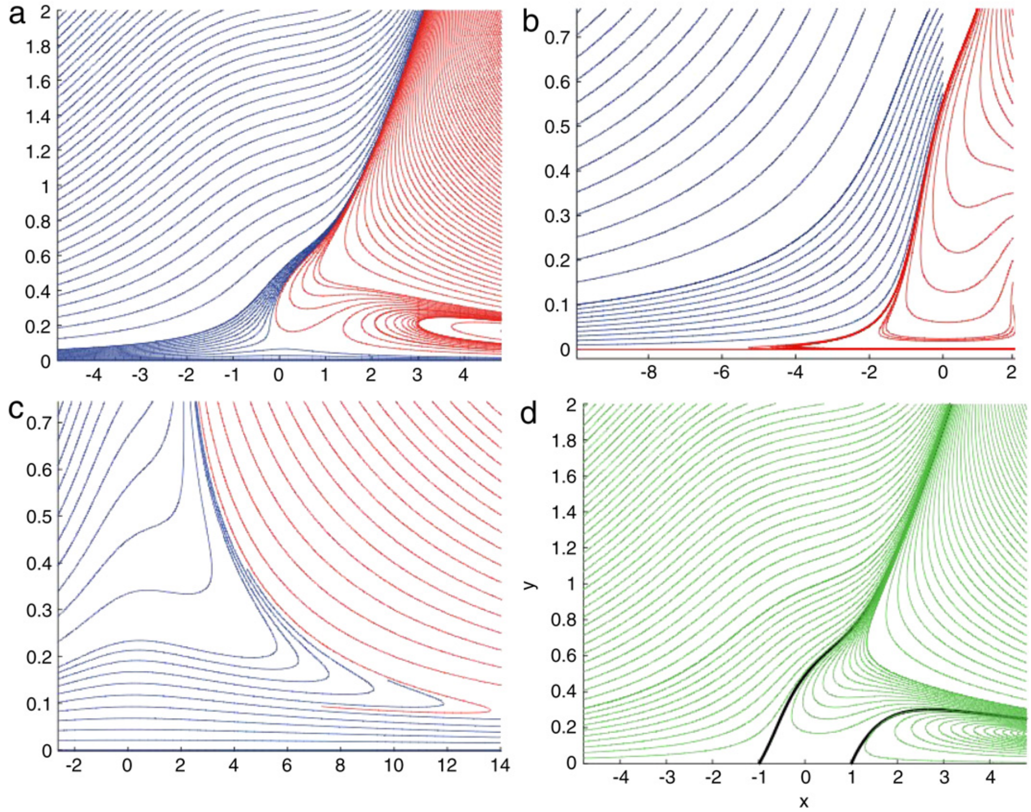

Fig. 7. (a) Steady streamlines for downstream moving wall with $U = 0.1$, (b) Same for an upstream moving wall with $U = -0.1$ (c) Same for downstream moving wall $U = 3.1$ (d) Instantaneous streamline pattern at $t = 0$ in the frame comoving with the wall for $U = 0.1$. In all cases $\alpha_0 = -1$, $\beta_0 = 1$ and $\gamma_0 = -5$.

Dropping the tilde and introducing the phase variable $\phi = Ut$, we obtain an unsteady velocity field $\mathbf{v}_s$ in the co-moving frame with components

$$\begin{aligned} u_s(\mathbf{x},\phi) &= \alpha_0 y + y^2 + \beta_0 (x+\phi)^2 y + \gamma_0 (x+\phi) y^2 - \frac{1}{3}\beta_0 y^3 + 15 y^4 \\ &\quad - (x+\phi)^3 y^2 + \frac{1}{2}\left[\frac{1}{6}\alpha_0\beta_0 + 1\right](x+\phi) y^4 + \frac{1}{30}\alpha_0\gamma_0 y^5 \\ v_s(\mathbf{x},\phi) &= -(x+\phi) y^2 \beta_0 - \frac{1}{3}\gamma_0 y^3 + (x+\phi)^2 y^3 - \frac{1}{10}\left[\frac{1}{6}\alpha_0\beta_0 + 1\right] y^5. \end{aligned} \tag{42}$$

Fig. 7(d) shows streamlines for the transformed velocity field $\mathbf{v}_s$ at $t = 0$. We observe two streamlines emanating from the wall: this means that wall shear is zero in the moving frame at points where these streamlines leave the wall. This suggests that contrary to the Sears–Tellionis argument, there may be on-wall signatures of moving separation near moving walls. This streamline pattern appears at $t = 0$ in the co-moving frame regardless of the wall-velocity U. For later times $t > 0$, this streamline pattern is of upstream-slipping type for a downstream moving wall ($U > 0$) and of downstream-slipping type for an upstream-moving wall ($U < 0$).

For the present flow, we have no fluctuation around the mean flow, and hence we have $\tilde{\mathbf{v}}_s(\mathbf{x},t) \equiv 0$ and $\mathbf{v}_s^0(\mathbf{x},\phi) \equiv \mathbf{v}_s(\mathbf{x},t)$, with U playing the role of ϵ. The zero wall shear point in the mean flow is given by

$$p(\phi) = -\delta - \phi, \qquad \delta = \sqrt{\frac{-\alpha_0}{\beta_0}}. \tag{43}$$

The conditions of Theorem 2 are satisfied whenever

$$\begin{aligned} &\langle A_x \rangle (p(\phi),0,\phi) = -2\beta_0\delta < 0, \\ &\langle C \rangle (p(\phi),0,\phi) - \langle A_x \rangle (p(\phi),0,\phi) - \epsilon \left| \frac{\langle A_\phi \rangle (p(\phi),0,\phi)}{\langle A_x \rangle (p(\phi),0,\phi)} \right| = 3\beta_0\delta - U > 0, \end{aligned}$$

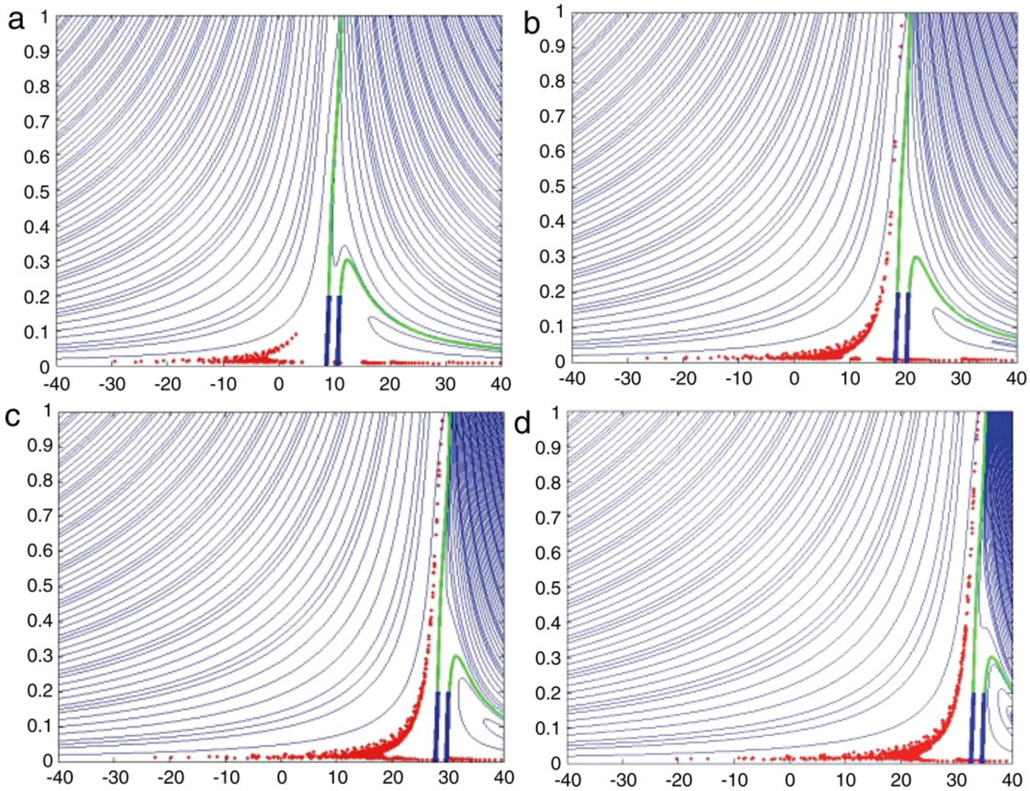

Fig. 8. Upstream moving wall with $U = -3$, $\alpha_0 = -1$, $\beta_0 = 1$, $\gamma_0 = -5$, satisfying condition (44). For this flow the instantaneous wall shear zeros (computed in the frame moving with the wall) coincide with the moving separation and reattachment location. Also shown are streamlines in blue and the separating and reattaching streamlines in green, along with their linear approximation in blue. Subplots (a)–(d) are taken at instants $t = 3.2$, $t = 6.4$, $t = 9.6$, and $t = 11.2$. (For interpretation of the references to colour in this figure legend, the reader is referred to the web version of this article.)

which hold provided that

$$U < 3\beta_0\delta. \tag{44}$$

For $U < 0$ (upstream-moving wall), this last condition is always satisfied. Furthermore, by (35), the slope of the separation spike at any time t_0 is given by the constant value

$$s(t_0) = \frac{1 - \gamma_0\delta + \delta^3}{3\beta_0\delta}.$$

Fig. 8 shows spike formation in the case of an upstream moving wall. Separation along the ghost manifold predicted by our theory is evident. The green streamline on the right generates an attachment, as its endpoint satisfies the conditions of Theorem 3.

Fig. 9 shows separating particle paths for a downstream-moving wall when the condition (44) is satisfied. In the case $U > 3\beta_0\delta$, Theorem 2 does not apply and hence we cannot predict whether or not $p(\phi)$ defined in (43) is a moving separation point.

Fig. 10 shows the case of a fast-moving wall that violates (44). Note that particles do not separate from the vicinity of the wall despite the presence of instantaneous wall shear zeros at $p(\phi)$. Fig. 7(c) shows steady streamlines in the lab frame for this wall speed. A weak jet-like streamline pattern is evident in agreement with the findings of Degani [5], who found similar streamline patterns corresponding to separation inhibition.

For intermediate wall speeds satisfying condition (44), we observe a change in the scale of separation. Fig. 11 shows a small-scale separation for wall speed $U = 1.2$. This underlines the fact that our separation criteria capture separation at all scales. While this universality is an advantage, it also a limitation: we cannot differentiate between local separation and large-scale boundary layer separation.

6.3. Slowly pulsating flow past a cylinder

In this section, we study separated flow past a stationary circular cylinder. There are two dimensionless parameters relevant to this flow, the Reynolds number $Re = 2U_m r/\nu$ and the Strouhal number $St = 2r/(U_m T)$, where r is the radius of cylinder, ν is the kinematic viscosity, U_m is the mean free stream velocity and T is the time period of von Kármán vortex shedding. The flow field

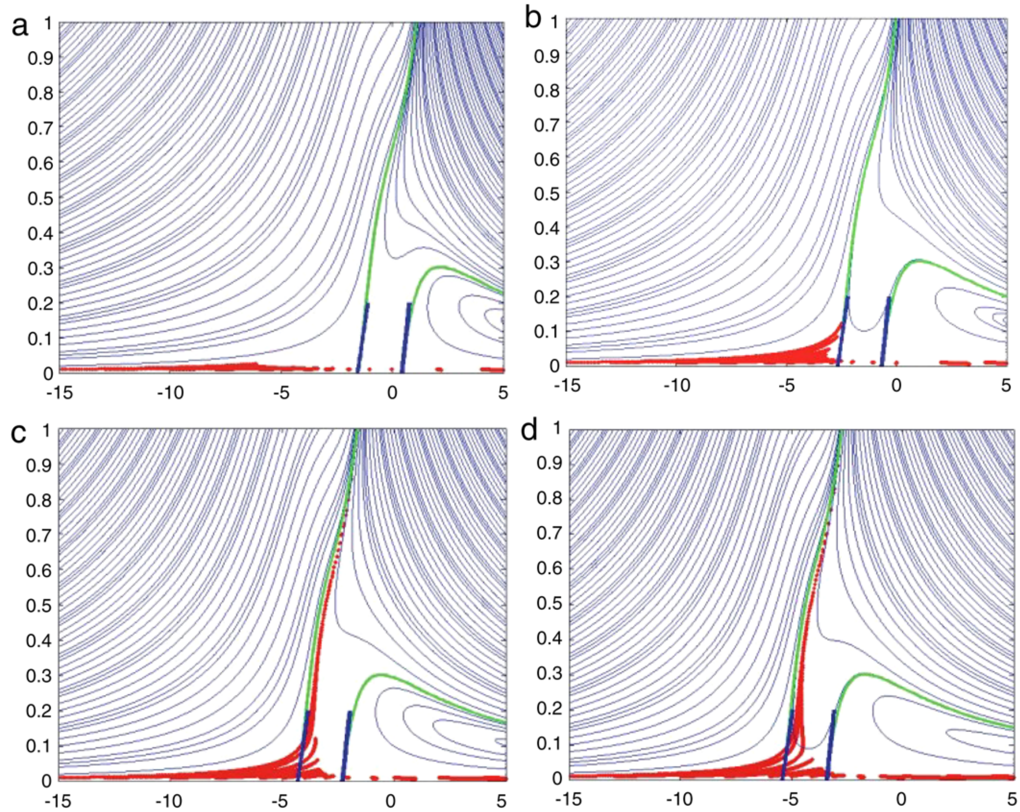

Fig. 9. Downstream moving wall with $U = 0.1$, $\alpha_0 = -1$, $\beta_0 = 1$, $\gamma_0 = -5$,satisfying condition (44). For this flow, the instantaneous wall shear zeros coincide with the moving separation and reattachment location. Also shown are streamlines in blue and separating and reattaching streamlines in green, along with their linear approximation in blue.Subplots (a)–(d) correspond to $t = 5.50$, $t = 16.50$, $t = 33.00$, and $t = 44.00$. (For interpretation of the references to colour in this figure legend, the reader is referred to the web version of this article.)

inherits the periodicity of vortex shedding, which itself is a function of the Reynolds number. We introduce a slow time scale in the system by perturbing the free stream velocity U as

$$U(t) = U_m + A\sin(\epsilon t), \tag{45}$$

where ϵ is a small parameter such that $2\pi/\epsilon \gg T$.

We solve the two-dimensional unsteady Navier–Stokes equations

$$\partial_t \mathbf{u} + \mathbf{u}\cdot\nabla\mathbf{u} = -\nabla p + \frac{1}{\mathrm{Re}}\nabla^2\mathbf{u},$$
$$\nabla\cdot\mathbf{u} = 0,$$

with p denoting pressure. Fig. 12 shows the computational domain and the reference frame, along with the O-type of mesh (generated by *GAMBIT*) used in our simulation. We use the spatial resolution recommended for this problem by [17].

The computational domain is partially bounded by two arcs of circle (B_i, B_o), one upstream of the cylinder and the other one downstream, both of the same radius R. There are also two horizontal segments (B_u, B_l) connecting the arcs and containing sectors of 10° span. The inclusion of these segments defines the transition region between inlet and outlet sections. For $R/(2r) > 75$, the solution is known to become independent of the location of the outer computational boundary [17,20]. For this reason we use $R/(2r) = 125$ in our simulation.

In the inflow section B_i, we use a Dirichlet-type boundary condition with the free stream velocity given by (45). For the outflow boundary B_o, the diffusion flux in the direction normal to the exit surface is taken to be zero for all flow variables. On horizontal segments B_u and B_l, zero normal velocity and zero normal gradient for all variables are prescribed. Finally, no-slip boundary condition is imposed on the cylinder. The initial condition for the computation is an impulsive start, i.e., at $t = 0$ the velocity field coincides with a potential flow past a stationary cylinder.

We used FLUENT to carry out the computation. Lift $C_L = L/\left(\frac{1}{2}\rho U^2 r\right)$ and drag $C_D = D/\left(\frac{1}{2}\rho U^2 r\right)$ coefficients (L and D are the lift and drag forces on the cylinder) are used as indicators of the convergence of the numerical solution. We set $U = 1$ m/s, $r = 1$ m, $A = 1$ m/s, $\epsilon = 0.01$/s, $\rho = 1$ Kg/m^3, and $\nu = 0.01$ m^2/s, so that $Re = 200$ and $St \approx 0.2$. In this case, $T \approx 10$ s is the

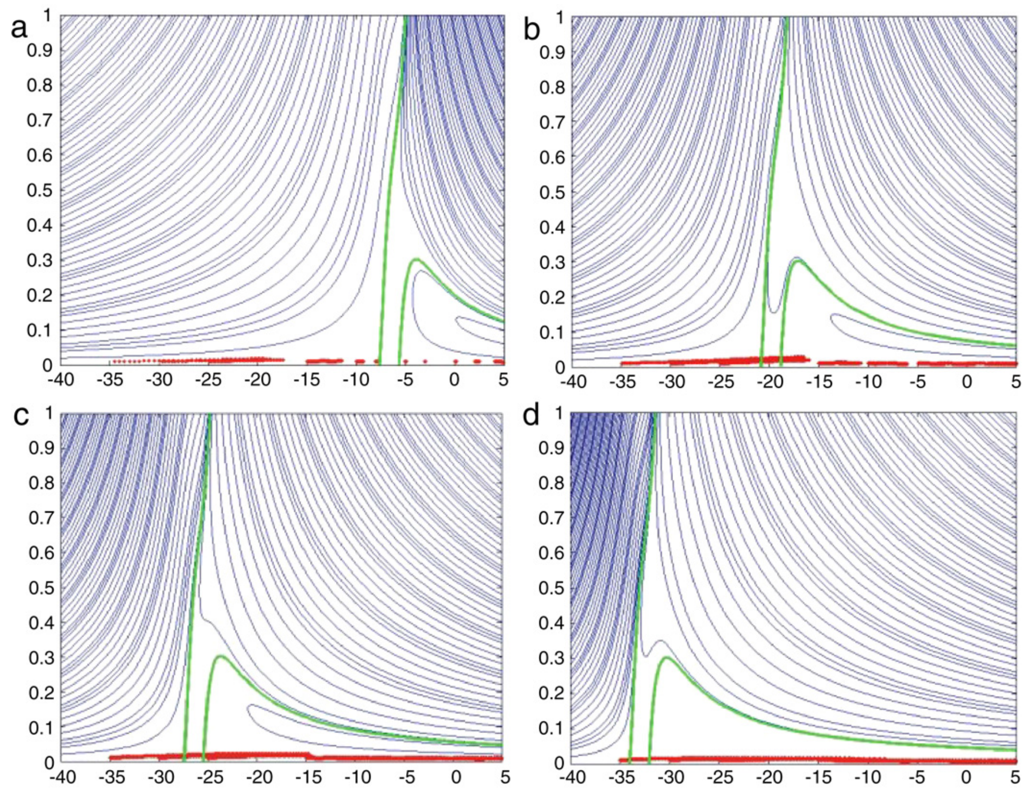

Fig. 10. Same as Fig. 9, but with $U = 3.1$, so that the condition (44) is violated. Particles are released at same location as for the case of Fig. 9. As can be seen, though there is an initial upwelling, there is no pronounced separation. Subplots correspond to $t = 3.05$, $t = 9.15$, $t = 12.20$, $t = 15.25$.

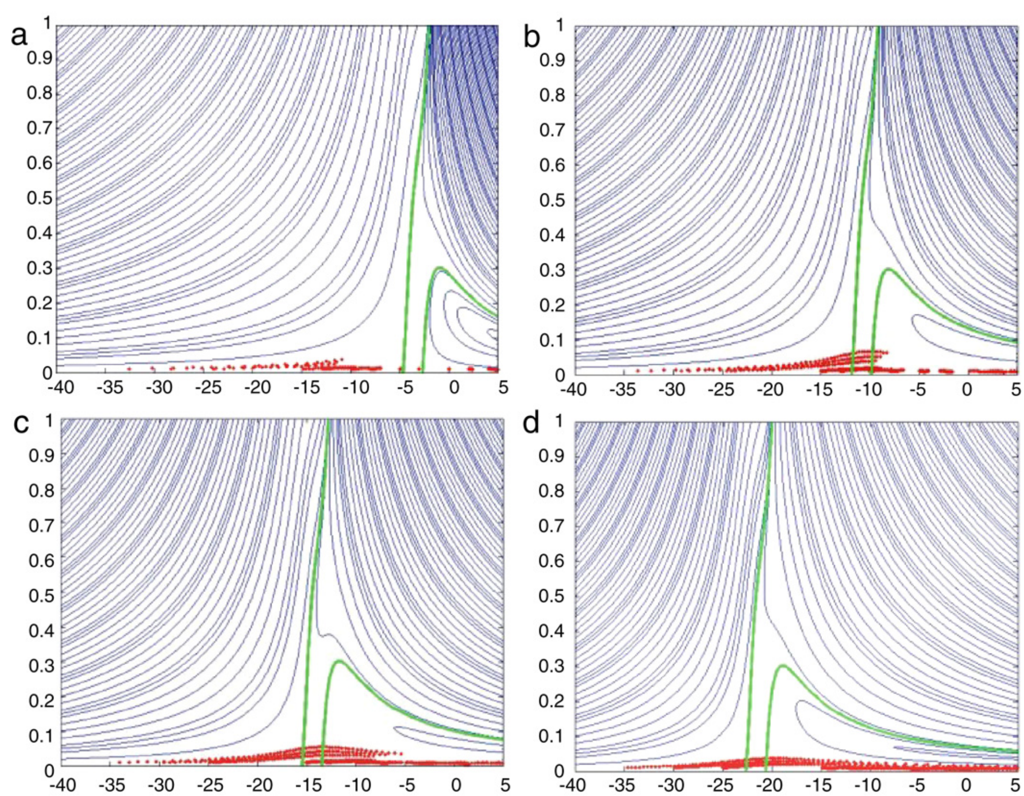

Fig. 11. Same as Fig. 9, but with $U = 1.2$, for which condition (44) is satisfied. Particles are released from the same location as in the case of Fig. 9. While there is an upwelling suggesting a small-scale separation, there is no pronounced spike formation. Subplots correspond to $t = 6$, $t = 9.0$, $t = 12.0$, and $t = 15.0$.

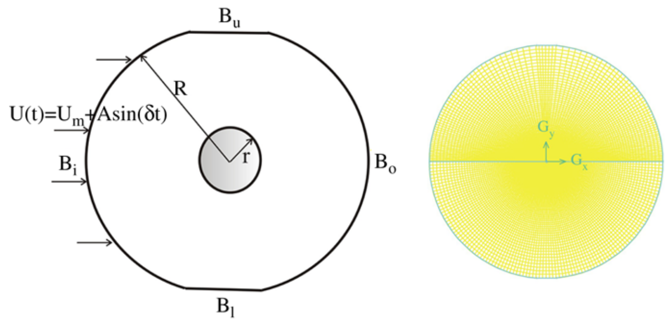

Fig. 12. (a) Computational domain and (b)Mesh.

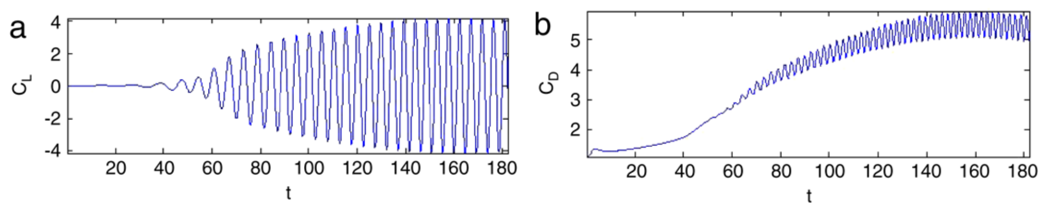

Fig. 13. Time history of (a) Lift coefficient and (b) Drag coefficient.

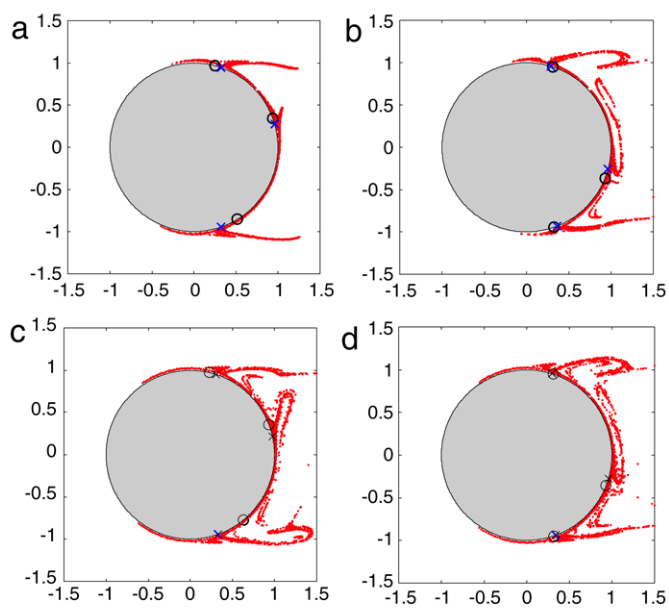

Fig. 14. Blue crosses show separation locations obtained from Theorem 2, while black circles are instantaneous wall-shear zeros. Subplots (a)–(d) correspond to times $t = 135.275$, $t = 142.275$, $t = 145.075$, and $t = 151.375$.

natural period of vortex shedding and $2\pi/\epsilon = 200\pi \gg T$. Fig. 13 shows the time history of drag and lift coefficients; the presence of a slow time scale is evident from these plots.

In order to implement dynamic averaging numerically, we used built-in functions of Matlab's Wavelet Toolbox. After trial and error, we found the *sym4* wavelet to be a good choice for a mother wavelet. Denoising was performed using a nonlinear multi-level soft thresholding, with the threshold value chosen based on the universal thresholding rule by Donoho & Johnstone [6]. Further details can be found in [8].

Numerical computation of $\langle A_\phi\rangle(p(\phi), 0, \phi)$ in the condition (34) requires further attention. Since

$$\epsilon\langle A_\phi\rangle(p(\phi), 0, \phi) = \langle\epsilon A_\phi\rangle(p(\phi), 0, \phi) = \langle A\rangle_t(x, 0, \epsilon t)\,|_{x=p(\epsilon t)}, \tag{46}$$

the condition (34) can be numerically computed without the explicit knowledge of ϵ. To evaluate the time derivative, we used finite differencing. Fig. 14 shows the predicted separation points along with particle paths. A closeup of separation as shown in Fig. 15, indicates that separation locations (blue crosses) obtained by application of Theorem 2 are able to capture separation well compared to instantaneous wall shear zeros (black circles). Fixed separation occurs at the top and bottom of the cylinder, while

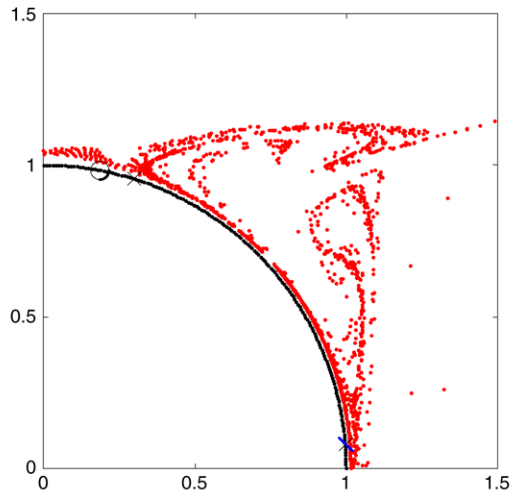

Fig. 15. Closeup of separation in the positive quadrant of cylinder.

moving separation is observed at the rear. Note that our moving separation criterion is also able to capture fixed separation locations, providing an unified approach to analyze separation in 2D unsteady fluid flows.

7. Conclusion

In this paper we have identified the root cause for moving pulses near non-hyperbolic critical manifolds of two dimensional non-autonomous dynamical systems with slow–fast time scales. We explained the existence of moving pulses by constructing a ghost manifold that lies off the critical manifold and yet can be predicted from its footprint on the critical manifold. Based on slowly evolving boundary layer dynamics near the critical manifold, we determined a sufficient condition for the existence of ghost manifolds. Wavelet based denoising was proposed to extract slow mean evolution.

We also showed how ghost manifolds arise in moving unsteady fluid flow separation over no-slip boundaries. Applying the conditions for locating ghost manifolds, we obtained a moving separation criterion, whose validity we illustrated on analytical models and on a numerical simulation of flow past a stationary cylinder. It appears that three-dimensional extensions of the present ghost manifold construction are possible, which should led to a characterization of moving separation in 3D unsteady fluid flows.

Acknowledgements

We thank Guustav Jacobs for useful discussions and suggestions. This work was supported by AFOSR grant F49620-03-1-0200 and NSF grant DMS-04-04845.

Appendix A. Averaging the modified system

To prove Theorem 1, we first observe that the fluctuations embodied by $\tilde{\mathbf{f}}$ in Eq. (17) can be transformed to higher-order terms by an appropriate version of the classical method of averaging. Specifically, we seek a near-identity transformation of the form

$$\mathbf{x} = \boldsymbol{\xi} + \epsilon \mathbf{w}(\boldsymbol{\xi}, \phi, t), \quad \boldsymbol{\xi} = (\xi, \lambda),$$

where $\mathbf{w} = (w_1, w_2)$ is a uniformly bounded function to be determined. Substitution into (17) gives

$$\begin{aligned}\dot{\mathbf{x}} &= \dot{\boldsymbol{\xi}} + \epsilon \nabla_{\boldsymbol{\xi}} \mathbf{w} \dot{\boldsymbol{\xi}} + \epsilon \partial_\phi \mathbf{w} \dot{\phi} + \epsilon \partial_t \mathbf{w} \\ &= \epsilon \mathbf{f}(\boldsymbol{\xi} + \epsilon \mathbf{w}, \phi, t) + \epsilon^2 \mathbf{g}(\boldsymbol{\xi} + \epsilon \mathbf{w}, \phi, t; \epsilon) + \mathcal{O}(\epsilon^3) \\ &= \epsilon \mathbf{f}(\boldsymbol{\xi}, \phi, t) + \epsilon^2 [\mathbf{g}(\boldsymbol{\xi}, \phi, t; 0) + \nabla_{\mathbf{x}} \mathbf{f}(\boldsymbol{\xi}, \phi, t)\mathbf{w}] + \mathcal{O}(\epsilon^3).\end{aligned} \tag{A.1}$$

From the transformed equation (A.1), we obtain

$$[\mathbf{I} + \epsilon \nabla_{\boldsymbol{\xi}} \mathbf{w}] \dot{\boldsymbol{\xi}} = \epsilon [\mathbf{f} - \partial_t \mathbf{w}] + \epsilon^2 \left[\mathbf{g}(\boldsymbol{\xi}, \phi, t; 0) + \nabla_{\mathbf{x}} \mathbf{f}(\boldsymbol{\xi}, \phi, t)\mathbf{w} - \Delta M(\lambda) \partial_\phi \mathbf{w} \right] + \mathcal{O}(\epsilon^3).$$

If $\|\nabla_{\boldsymbol{\xi}} \mathbf{w}\|$ remains uniformly bounded for all $t \leq t_0$, then for small enough ϵ, we can write

$$[\mathbf{I} + \epsilon \nabla_{\boldsymbol{\xi}} \mathbf{w}]^{-1} = \mathbf{I} - \epsilon \nabla_{\boldsymbol{\xi}} \mathbf{w} + \mathcal{O}(\epsilon^2), \tag{A.2}$$

from which we obtain

$$\dot{\boldsymbol{\xi}} = [\mathbf{I} + \epsilon\nabla_{\boldsymbol{\xi}}\mathbf{w}]^{-1}\left\{\epsilon[\mathbf{f} - \partial_t\mathbf{w}] + \epsilon^2[\mathbf{g}(\boldsymbol{\xi}, \phi, t; 0) + \nabla_{\mathbf{x}}\mathbf{f}(\boldsymbol{\xi}, \phi, t)\mathbf{w} - \Delta M(\lambda)\partial_\phi\mathbf{w}] + \mathcal{O}(\epsilon^3)\right\},$$
$$= \epsilon[\mathbf{f} - \partial_t\mathbf{w}] + \epsilon^2\left[\mathbf{g}(\boldsymbol{\xi}, \phi, t; 0) + \nabla_{\mathbf{x}}\mathbf{f}(\boldsymbol{\xi}, \phi, t)\mathbf{w} - \Delta M(\lambda)\partial_\phi\mathbf{w} - \nabla_{\boldsymbol{\xi}}\mathbf{w}(\mathbf{f} - \partial_t\mathbf{w})\right] + \mathcal{O}(\epsilon^3).$$

By choosing

$$\mathbf{w}(\boldsymbol{\xi}, \phi, t) = \begin{pmatrix} w_1(\boldsymbol{\xi}, \phi, t) \\ w_2(\boldsymbol{\xi}, \phi, t) \end{pmatrix}\int_{t_0}^{t}[\mathbf{f}(\boldsymbol{\xi}, \phi, \tau) - \mathbf{f}^0(\boldsymbol{\xi}, \phi)]\mathrm{d}\tau, \tag{A.3}$$

we ensure uniform boundedness of $\mathbf{w}$ and $\|\nabla_{\boldsymbol{\xi}}\mathbf{w}\|$ (cf. assumption (11)), and obtain the first-order averaged form of (17) as

$$\dot{\boldsymbol{\xi}} = \epsilon\mathbf{f}^0(\boldsymbol{\xi}, \phi) + \epsilon^2[\mathbf{F}(\boldsymbol{\xi}, \phi, t) - \Delta\partial_\phi\mathbf{w}M(\lambda)] + \mathcal{O}(\epsilon^3),$$
$$\dot{\phi} = M(\lambda + \epsilon w_2) = \epsilon\Delta M(\lambda) + \mathcal{O}(\epsilon^2), \tag{A.4}$$

where

$$\mathbf{F}(\boldsymbol{\xi}, \phi, t) = \begin{pmatrix} \lambda^2 F(\xi, \phi, t) \\ \lambda^3 G(\xi, \phi, t) \end{pmatrix} = \mathbf{g}(\boldsymbol{\xi}, \phi, t; 0) + (\nabla_{\mathbf{x}}\mathbf{f})\,\mathbf{w} - \left(\nabla_{\boldsymbol{\xi}}\mathbf{w}\right)\mathbf{f}^0, \tag{A.5}$$

with

$$F(\xi, \phi, t) = g_1(\xi, \phi, t) + [\partial_x f_1(\xi, \phi, t) - f_2^0(\xi, \phi)]\varphi + f_1(\xi, \phi, t)\psi - f_1^0(\xi, \phi)\partial_\xi\varphi,$$
$$G(\xi, \phi, t) = g_2(\xi, \phi, t) + 2[f_2(\xi, \phi, t) - f_2^0(\xi, \phi)]\psi + \partial_x f_2(\xi, \phi, t)\varphi - f_1^0(\xi, \phi)\partial_\xi\psi,$$
$$\varphi(\xi, \phi, t) = \int_{t_0}^{t}[f_1(\xi, \phi, \tau) - f_1^0(\xi, \phi)]\mathrm{d}\tau, \quad \psi(\xi, \phi, t) = \int_{t_0}^{t}[f_2(\xi, \phi, \tau) - f_2^0(\xi, \phi)]\mathrm{d}\tau,$$
$$\mathbf{w}(\boldsymbol{\xi}, \phi, t) = \begin{pmatrix} w_1 \\ w_2 \end{pmatrix} = \begin{pmatrix} \lambda\varphi(\xi, \phi, t) \\ \lambda^2\psi(\xi, \phi, t) \end{pmatrix}.$$

Appendix B. The Wasewski principle

We first recall a topological result, the Wasewski principle, in its general form; we shall apply this principle below in constructing an unstable manifold for the averaged Eq. (A.4) obtained above.

Suppose that Ω is an open set in $\mathbb{R}^n$, $f : \Omega \to \mathbb{R}^n$ is continuous and the flow map $\phi^t(\mathbf{x}_0)$: $\mathbf{x}_0 \mapsto \mathbf{x}(t; \mathbf{x}_0)$ of

$$\dot{\mathbf{x}} = f(\mathbf{x}), \tag{B.1}$$

depends continuously on the initial conditions $\mathbf{x}_0$. We denote the closure of a set $A \subset \Omega$ by $cl(A)$ and define

$$\Phi(\mathbf{x}_0, \mathcal{I}) = \{\phi^t(\mathbf{x}_0) \mid t \in \mathcal{I}\},$$

where $\mathcal{I} \subset \mathbf{R}$. The following formulation of *Wasewski* principle is taken from ([2]).

Let $W \subset \Omega$ be any set and consider the sets

$$W^{ev} = \{\mathbf{x} \in W \mid \phi^t(\mathbf{x}) \notin W \text{ for some } t > 0\},$$
$$W^{im} = \{\mathbf{x} \in W \mid \Phi(\mathbf{x}, [0, t]) \not\subset W, \forall t > 0\}.$$

Clearly we have $W^{im} \subset W^{ev}$.

The set W is called a forward-time *Wasewski* set if the following conditions are satisfied:

(1) If $\mathbf{x} \in W$ and $\Phi(\mathbf{x}, [0, t]) \subset cl(W)$, then $\Phi(\mathbf{x}, [0, t]) \subset W$,
(2) W^{im} is relatively closed in W^{ev}, i.e., if a Cauchy sequence in W^{im} converges to point $p \in W^{ev}$, then we must have $p \in W^{im}$.

Wasewski principle: If W is a Wasewski set, then W^{im} is a *strong deformation retract* of W^{ev}, and W^{ev} is relatively open in W.

The proof of above result follows from continuity of the flow map $\phi^t(\mathbf{x})$ (see [2] for details). An important quantity introduced in the proof is the first-exit-time map $\tau : W^{ev} \to \mathbf{R}$, defined as

$$\tau(\mathbf{x}) = \sup\{t \geq 0 \mid \Phi([0, t], \mathbf{x}) \subset W\}.$$

By definition of W^{ev}, the map $\tau(\mathbf{x})$ takes finite values. By continuity of the flow map $\phi^t(\mathbf{x}_0)$, we have $\Phi(\mathbf{x}, [0, \tau(\mathbf{x})]) \subset cl(W)$. Thus, by property (1) of W, $\phi^{\tau(\mathbf{x})}(\mathbf{x}) \in W$. Now from the definition of τ, we have $\phi^{\tau(\mathbf{x})}(\mathbf{x}) \in W^{im}$ and $\tau(\mathbf{x}) = 0$ for $\mathbf{x} \in W^{im}$. This leads to the following corollary.

Corollary. *The Wasewski map* $\Gamma : W^{ev} \to W^{im}$ *defined as*

$$\Gamma(\mathbf{x}) = \phi^{\tau(\mathbf{x})}(\mathbf{x}), \tag{B.2}$$

is continuous.

Appendix C. Unstable manifold for system (17)

The first-order averaged equation (A.4) can be written as

$$\begin{aligned}
\dot{\xi} &= \epsilon\lambda[f_1^0(\xi,\phi) + \mathcal{O}(\epsilon\lambda)] + \mathcal{O}(\epsilon^2\lambda) + \mathcal{O}(\epsilon^3\lambda^3),\\
\dot{\lambda} &= \epsilon\lambda^2[f_2^0(\xi,\phi) + \mathcal{O}(\epsilon\lambda)] + \mathcal{O}(\epsilon^2\lambda^2) + \mathcal{O}(\epsilon^3\lambda^4),\\
\dot{\phi} &= \epsilon\Delta M(\lambda).
\end{aligned} \tag{C.1}$$

We introduce the change of coordinates

$$\zeta = \xi - p(\phi),$$

with $p(\phi)$ satisfying (16), the new equations of motion become

$$\begin{aligned}
\dot{\zeta} &= -\epsilon\Delta p'(\phi)M(\lambda) + \epsilon\lambda[\zeta\partial_x f_1^0(p(\phi),\phi) + \mathcal{O}(\epsilon\lambda) + \mathcal{O}(\zeta^2)] + \mathcal{O}(\epsilon^2\lambda) + \mathcal{O}(\epsilon^3\lambda^3),\\
\dot{\lambda} &= \epsilon\lambda^2[f_2^0(p(\phi),\phi) + \mathcal{O}(\epsilon\lambda) + \mathcal{O}(\zeta)] + \mathcal{O}(\epsilon^2\lambda^2) + \mathcal{O}(\epsilon^3\lambda^4),\\
\dot{\phi} &= \epsilon\Delta M(\lambda).
\end{aligned} \tag{C.2}$$

We also define the wedge-shaped set

$$W = \{(\zeta,\lambda,\phi) \mid \ |\zeta| \le \lambda,\ \lambda \in [0,h(\phi)],\ \phi \in \mathcal{I}\}, \tag{C.3}$$

along the curve $\mathcal{C}$, where the ϕ–dependent height, $h(\phi)$, of W is yet to be chosen.

Note that W is bounded by the surfaces

$$\begin{aligned}
S^+ &= \{(\zeta,\lambda,\phi) \mid \zeta = \lambda,\ \lambda \in [0,h(\phi)],\ \phi \in \mathcal{I}\},\\
S^- &= \{(\zeta,\lambda,\phi) \mid \zeta = -\lambda,\ \lambda \in [0,h(\phi)],\ \phi \in \mathcal{I}\},\\
T &= \{(\zeta,h(\phi),\phi) \mid |\zeta| \le h(\phi), \phi \in \mathcal{I}\},\\
L &= \{(\zeta,\lambda,\phi_0) \mid |\zeta| \le \lambda,\ \lambda \in [0,h(\phi_0)]\}.
\end{aligned}$$

We observe the following:

1. Along $S^{\pm}$, the outer normal to W is given by $\mathbf{n}_{S^{\pm}} = \frac{1}{\sqrt{2}}(\pm 1,-1,0)$ and hence on $S^{\pm}$, the right-hand-side $\mathbf{v}^m$ of system (C.2) satisfies

$$\mathbf{v}^m \cdot \mathbf{n}_{S^{\pm}}\big|_{S^{\pm}} = \pm\epsilon\Delta p'(\phi)M(\lambda) + \epsilon\lambda^2\{[\partial_x f_1^0(p(\phi),\phi) - f_2^0(p(\phi),\phi)] + \mathcal{O}(\epsilon) + \mathcal{O}(\lambda)\}.$$

- For $z^* \le \lambda \le h(\phi)$, we have

$$\begin{aligned}
\mathbf{v}^m \cdot \mathbf{n}_{S^{\pm}}\big|_{S^{\pm}} &= \pm\epsilon\Delta p'(\phi) + \epsilon\lambda^2\left[\partial_x f_1^0(p(\phi),\phi) - f_2^0(p(\phi),\phi)\right] + \mathcal{O}(\epsilon\lambda)\\
&< \epsilon\Delta\left|p'(\phi)\right| + \epsilon(z^*)^2\left[\partial_x f_1^0(p(\phi),\phi) - f_2^0(p(\phi),\phi)\right] + \epsilon h(\phi)K_1.
\end{aligned}$$

Fixing

$$\Delta = 1, \qquad z^* = \frac{1}{\sqrt{\epsilon}}, \tag{C.4}$$

we obtain, under the condition (19),

$$\begin{aligned}
\mathbf{v}^m \cdot \mathbf{n}_{S^{\pm}}\big|_{S^{\pm}} &< -\left[f_2^0(p(\phi),\phi) - \partial_x f_1^0(p(\phi),\phi) - \epsilon\left|p'(\phi)\right|\right] + \epsilon h(\phi)K_1\\
&< 0,
\end{aligned} \tag{C.5}$$

for all $\phi \in \mathcal{I}$, appropriate $K_1 > 0$ and

$$h(\phi) \le H_1 = \frac{\inf_{\phi\in\mathcal{I}}\left[f_2^0(p(\phi),\phi) - \partial_x f_1^0(p(\phi),\phi) - \epsilon\left|p'(\phi)\right|\right]}{2\epsilon K_1} = \frac{C_1}{2\epsilon K_1}, \tag{C.6}$$

provided that

$$z^* = \left\{\frac{1}{\epsilon}\right\}^{\frac{1}{2}} < h(\phi) \le H_1 = \frac{C_1}{2\epsilon K_1}, \tag{C.7}$$

or

$$\sqrt{\epsilon} < \frac{C_1}{2K_1} \Longrightarrow \epsilon \leq \left\{ \frac{C_1}{2K_1} \right\}^2. \tag{C.8}$$

- For $\frac{z^*}{q} < \lambda < z^*$, following the above steps and using (C.4), we again obtain

$$\begin{aligned} \mathbf{v}^m \cdot \mathbf{n}_{S^\pm}\big|_{S^\pm} &= \pm\epsilon p'(\phi)M(\lambda) + \epsilon\lambda^2 \left[\partial_x f_1^0(p(\phi),\phi) - f_2^0(p(\phi),\phi)\right] + \mathcal{O}(\epsilon\lambda) \\ &< \epsilon \left|p'(\phi)\right| + \epsilon \left(\frac{z^*}{q}\right)^2 \left[\partial_x f_1^0(p(\phi),\phi) - f_2^0(p(\phi),\phi)\right] + \mathcal{O}(\epsilon\lambda) \\ &< -\left\{ \frac{1}{q^2}\left[f_2^0(p(\phi),\phi) - \partial_x f_1^0(p(\phi),\phi)\right] - \epsilon\left|p'(\phi)\right| \right\} + \epsilon h(\phi) K_2 \\ &< 0, \end{aligned} \tag{C.9}$$

for appropriate $K_2 > 0$ and $q = 1 + \delta$ with $0 < \delta \ll 1$, provided that ϵ and $h(\phi)$ is small enough.

- For $0 < \lambda \leq \frac{z^*}{q}$, we obtain similarly from (19) that

$$\begin{aligned} \mathbf{v}^m \cdot \mathbf{n}_{S^\pm}\big|_{S^\pm} &< -\epsilon\lambda^2 \{[f_2^0(p(\phi),\phi) - \partial_x f_1^0(p(\phi),\phi)] + \mathcal{O}(\epsilon) + \mathcal{O}(\lambda)\} \\ &< -\epsilon\lambda^2 \{[f_2^0(p(\phi),\phi) - \partial_x f_1^0(p(\phi),\phi)] + \epsilon K_3 + h(\phi) K_4\} \\ &< 0, \end{aligned} \tag{C.10}$$

for appropriate $K_3, K_4 > 0$ provided that ϵ and $h(\phi)$ are small enough.

2. Along the boundary segment T of W, the outer normal is given by $\mathbf{n}_T = (0,0,1)$, and

$$\begin{aligned} \mathbf{v}^m \cdot \mathbf{n}_T\big|_T &= \epsilon h^2(\phi)[f_2^0(p(\phi),\phi) + \mathcal{O}(\epsilon h(\phi)) + \mathcal{O}(\zeta)], \\ &> \epsilon h^2(\phi)[f_2^0(p(\phi),\phi) - \epsilon h(\phi) K_2 - h(\phi) K_3] \\ &> 0, \end{aligned} \tag{C.11}$$

for appropriate $K_2, K_3 > 0$, and small enough $\epsilon > 0$ and h_ϕ.

3. Along L, the outer normal is given by $\mathbf{n}_L = (0,0,1)$, and hence, by (C.4), we have

$$\mathbf{v}^m \cdot \mathbf{n}_L\big|_L = \epsilon M(\lambda + \epsilon w_2) \geq 0. \tag{C.12}$$

We now fix $h(\phi) = h > 0$, $\epsilon > 0$ small enough so that estimates (C.5)–(C.12) for system (C.2) all hold for all $\phi \in \mathcal{I} = (-\infty, \phi_0)$, where $\phi_0 = \epsilon t_0$. We then rewrite (C.2) as an autonomous dynamical system on the extended phase space of the $(\zeta, \lambda, \phi, t)$ variables as follows:

$$\begin{aligned} \dot{\zeta} &= -\epsilon\Delta p'(\phi)M(\lambda) + \epsilon\lambda[\zeta\,\partial_x f_1^0(p(\phi),\phi) + \mathcal{O}(\epsilon\lambda) + \mathcal{O}(\zeta^2)] + \mathcal{O}(\epsilon^2\lambda) + \mathcal{O}(\epsilon^3\lambda^3), \\ \dot{\lambda} &= \epsilon\lambda^2[f_2^0(p(\phi),\phi) + \mathcal{O}(\epsilon\lambda) + \mathcal{O}(\zeta)] + \mathcal{O}(\epsilon^2\lambda^2) + \mathcal{O}(\epsilon^3\lambda^4), \\ \dot{\phi} &= \epsilon\Delta M(\lambda), \\ \dot{t} &= 1. \end{aligned}$$

For this system, we define the set

$$\mathcal{W} = W \times (-\infty, t_0),$$

the extension of the cone W defined in (C.3).

Observe that by estimates (C.5)–(C.12), the set of initial conditions $(\zeta_0, \lambda_0, \phi_0, t_0)$ that immediately leave $\mathcal{W}$ in *backward* time is given by

$$\mathcal{W}^{im} = \left\{(\zeta,\lambda,\phi,t) \in \mathcal{W} \mid \lambda > 0,\ (\zeta,\lambda,\phi) \in S^+ \cup S^-\right\}, \tag{C.13}$$

which is a union of the two disjoint components $\left(S^+ \cap \{\lambda > 0\}\right) \times (-\infty, t_0]$ and $\left(S^- \cap \{\lambda > 0\}\right) \times (-\infty, t_0]$.

Assume that $\mathcal{W}^{ev} = \mathcal{W}$, i.e., all the initial conditions eventually leave $\mathcal{W}$ in backward time. Then $\mathcal{W}$ qualifies as a backward time Wasewski set, since

1. $\mathrm{cl}(\mathcal{W}) = \mathcal{W}$,
2. $\mathcal{W}^{im}$ is a relatively closed subset of $\mathcal{W}^{ev}$. Indeed, Cauchy sequences in $\mathcal{W}^{im}$ that converge to $\mathcal{C}$ (given by $\zeta = 0, \lambda = 0$), have their limit points outside $\mathcal{W}^{im}$ and $\mathcal{W}^{ev}$. All other sequences in $\mathcal{W}^{im}$ converge to points within $\mathcal{W}^{im}$ and those points are in $\mathcal{W}^{ev}$, since $\mathcal{W}^{im} \subset \mathcal{W}^{im}$ by definition.

Thus, by the Wasewski principle, the *Wasweski map Γ* defined in (B.2) is continuous, which is a contradiction, because Γ maps the connected set $\mathcal{W}^{ev}$ into the disconnected set $\mathcal{W}^{im}$. Therefore, we conclude that $\mathcal{W}^{ev} \neq \mathcal{W}$ and there exists a nonempty set $\tilde{\mathcal{W}}_\epsilon^\infty$ of solutions which stay in $\mathcal{W}$ for all backward times, i.e.. for $(-\infty, t_0]$. Also

1. $\tilde{\mathcal{W}}_{\epsilon}^{\infty}$ is a two dimensional set,
2. $\tilde{\mathcal{W}}_{\epsilon}^{\infty}$ extends to the top boundary $T \times (-\infty, t_0)$ of the Wasewki set, $\mathcal{W}$, and
3. $\tilde{\mathcal{W}}_{\epsilon}^{\infty}$ is necessarily smooth in t, because it is composed of trajectories that are smooth in t.

Next we want to argue that all solutions in $\tilde{\mathcal{W}}_{\epsilon}^{\infty}$ tend to $\zeta = \lambda = 0$ in backward time. Consider a specific initial condition $(\zeta_0, \lambda_0, \phi_0, t_0) \in \tilde{\mathcal{W}}_{\epsilon}^{\infty}$, and denote the trajectory emanating from this initial position by $(\zeta(t), \lambda(t), \phi(t))$. Along this trajectory, the λ-component of system (C.2) can be re-written as

$$\dot{\lambda} = \epsilon\lambda^2[f_2^0(p(\phi), \phi) + \zeta m_1(\zeta, \lambda, \phi, t) + \epsilon m_2(\zeta, \lambda, \phi, t)], \tag{C.14}$$

for some appropriate smooth functions m_1 and m_2. Direct integration gives

$$\begin{aligned}\lambda(t) &= \frac{\lambda_0}{1 + \epsilon\lambda_0 \int_t^{t_0}[f_2^0(p(\phi), \phi) + \zeta m_1(\zeta, \lambda, \phi, \tau) + \epsilon m_2(\zeta, \lambda, \phi, t)]\,\mathrm{d}\tau}, \\ &\le \frac{\lambda_0}{1 + \epsilon\lambda_0 \int_t^{t_0}[f_2^0(p(\phi), \phi) - H|m_1(\zeta, \lambda, \phi, \tau)| - \epsilon|m_2(\zeta, \lambda, \phi, t)|]\,\mathrm{d}\tau},\end{aligned}$$

with H being a uniform upper bound for $h(\phi)$. The above inequality holds for all $t \in (-\infty, t_0]$, because the trajectory we consider stays in $\mathcal{W}$ for all backward times. Making ϵ and H small enough, the uniform boundedness of $m_k(\zeta, \lambda, \phi, \tau)$ leads to the estimate

$$\lambda(t) \le \frac{\lambda_0}{1 + \frac{1}{2}\epsilon\lambda_0 \int_t^{t_0} \inf\limits_{\phi\in\mathcal{I}} f_2^0(p(\phi), \phi)\,\mathrm{d}\tau} = \frac{\lambda_0}{1 + \epsilon\lambda_0 c_2(t_0 - t)/2},$$

which implies that

$$\lim_{t\to-\infty} \lambda(t) = 0.$$

Therefore, trajectories that never leave $\mathcal{W}$ in backward time will necessary converge to the $\lambda = 0$ boundary of $\mathcal{W}$. By definition of $\mathcal{W}$, however, this convergence in the λ direction implies

$$\lim_{t\to-\infty} \zeta(t) = 0.$$

We therefore conclude that all trajectories in $\tilde{\mathcal{W}}_{\epsilon}^{\infty}$ converge to the set $\lambda = \zeta = 0$ (i.e., the curve $\mathcal{C}$) in backward time, thus $\tilde{\mathcal{W}}_{\epsilon}^{\infty}$ is an unstable manifold for $\mathcal{C}$ for all $t \le t_0$.

Appendix D. Slope of the unstable manifold for $\Delta = 0$

In this section we determine a slope formula that can be used to linearly approximate $\mathcal{W}_{\epsilon}^{\infty}$. By the structure of the steady adiabatic limit (14) of first order averaged normal form (A.4), we obtain $(x, y) = (p(\phi), y)$ as a first order approximation for $\mathcal{W}_{\epsilon}^{\infty}$. Following the approach developed in [15] for fixed unsteady separation in fluid flows, the approximation for $\mathcal{W}_{\epsilon}^{\infty}$ can be refined by a second order averaging.

As in case of first-order averaging, we eliminate the oscillatory part of $\mathbf{F}$ in Eq. (A.4) by seeking a near-identity coordinate change of the form

$$\boldsymbol{\xi} = \boldsymbol{\eta} + \epsilon^2\mathbf{h}(\boldsymbol{\eta}, \phi, t), \quad \boldsymbol{\eta} = (\eta, \mu),$$

where, $\mathbf{h} = (h_1, h_2)$ is a uniformly bounded function to be specified later. The above coordinate applied to system (A.4) with $\Delta = 0$ gives

$$\begin{aligned}\dot{\boldsymbol{\xi}} &= \dot{\boldsymbol{\eta}} + \epsilon^2\left(\nabla_{\boldsymbol{\eta}}\mathbf{h}\right)\dot{\boldsymbol{\eta}} + \epsilon^2\left(\partial_\phi\mathbf{h}\right)\dot{\phi} + \epsilon^2\partial_t\mathbf{h}, \\ &= \epsilon\mathbf{f}^0(\boldsymbol{\eta} + \epsilon^2\mathbf{h}, \phi) + \epsilon^2\mathbf{F}(\boldsymbol{\eta} + \epsilon^2\mathbf{h}, \phi, t) + \mathcal{O}(\epsilon^3), \\ &= \epsilon\mathbf{f}^0(\boldsymbol{\eta}, \phi) + \epsilon^2\mathbf{F}(\boldsymbol{\eta}, \phi, t) + \mathcal{O}(\epsilon^3),\end{aligned} \tag{D.1}$$

leading to

$$[\mathbf{I} + \epsilon^2\nabla_{\boldsymbol{\eta}}\mathbf{h}]\dot{\boldsymbol{\eta}} = \epsilon\mathbf{f}^0(\boldsymbol{\eta}, \phi) + \epsilon^2[\mathbf{F}(\boldsymbol{\eta}, \phi, t - \partial_t\mathbf{h})] + \mathcal{O}(\epsilon^3). \tag{D.2}$$

If $\|\nabla_{\boldsymbol{\eta}}\mathbf{h}\|$ remains uniformly bounded for all $t \le t_0$, then for small enough ϵ, the operator $[\mathbf{I} + \epsilon^2\nabla_{\boldsymbol{\eta}}\mathbf{h}]$ is invertible, and hence (D.2) can be written as

$$\begin{aligned}\dot{\boldsymbol{\eta}} &= [\mathbf{I} + \epsilon^2\nabla_{\boldsymbol{\eta}}\mathbf{h}]^{-1}\left\{\epsilon\mathbf{f}^0(\boldsymbol{\eta}, \phi) + \epsilon^2[\mathbf{F}(\boldsymbol{\eta}, \phi, t) - \partial_t\mathbf{h}] + \mathcal{O}(\epsilon^3)\right\}, \\ &= \epsilon\mathbf{f}^0(\boldsymbol{\eta}, \phi) + \epsilon^2[\mathbf{F}(\boldsymbol{\eta}, \phi, t) - \partial_t\mathbf{h}] + \mathcal{O}(\epsilon^3).\end{aligned} \tag{D.3}$$

We recall that we have set $\Delta = 0$, therefore $\phi =$ const. by (A.4).

Assume that $\mathbf{F}$ (A.5) admits a decomposition of the form

$$\mathbf{F}(\boldsymbol{\xi}, \phi, t) = \mathbf{F}^0(\boldsymbol{\xi}, \phi) + \tilde{\mathbf{F}}(\boldsymbol{\xi}, \phi, t), \quad \lim_{T\to\infty} \frac{1}{T} \int_{t_0-T}^{t_0} \tilde{\mathbf{F}}(\boldsymbol{\xi}, \phi, t)\mathrm{d}t = 0.$$

Then by choosing

$$\mathbf{h}(\boldsymbol{\eta}, \phi, t) = \int_{t_0}^{t} [\mathbf{F}(\boldsymbol{\eta}, \phi, t) - \mathbf{F}^0(\boldsymbol{\eta}, \phi)]\, \mathrm{d}\tau, \tag{D.4}$$

we obtain from (D.3) the second-order averaged normal form

$$\dot{\eta} = \epsilon\mu \left[f_1^0(\eta, \phi) + \epsilon\mu F^0(\eta, \phi) \right] + \mathcal{O}(\epsilon^3),$$
$$\dot{\mu} = \epsilon\mu^2 \left[f_2^0(\eta, \phi) + \epsilon\mu G^0(\eta, \phi) \right] + \mathcal{O}(\epsilon^3).$$

Rescaling time by letting $\mathrm{d}\tau/\mathrm{d}t = \epsilon\mu(t)$ and ignoring higher-order terms, we obtain the system

$$\eta' = f_1^0(\eta, \phi) + \epsilon\mu F^0(\eta, \phi),$$
$$\mu' = \mu \left[f_2^0(\eta, \phi) + \epsilon\mu G^0(\eta, \phi) \right].$$

Under the conditions of Theorem 1, the above system has an hyperbolic fixed point $(p(\phi), 0)$ for every constant $\phi \in \mathcal{I}$ with an associated one dimensional unstable manifold. The unstable manifold at $\phi \in \mathcal{I}$ is tangent to the unstable eigenvector

$$\mathbf{e}(\phi) = \begin{pmatrix} \epsilon F^0(p(\phi), \phi) \\ f_2^0(p(\phi), \phi) - \partial_x f_1^0(p(\phi), \phi) \end{pmatrix}. \tag{D.5}$$

Recalling that

$$(\eta, \mu) = (\xi, \lambda) + \mathcal{O}(\epsilon^2) = (x, z) + \mathcal{O}(\epsilon) = (x, y/\epsilon) + \mathcal{O}(\epsilon),$$

we find from (D.5) that the slope of $\mathcal{W}_\epsilon^\infty$ relative to the normal of $\mathcal{S}$ becomes (21).

References

[1] C. Chicone, Ordinary Differential Equations with Applications, Springer, 2006.
[2] C. Conley, Isolated Invariant Set and Morse Index, AMS, 1970.
[3] B.T. Darling, D.M. Dennison, The water vapor molecule, Phys. Rev. 57 (1997) 128–139.
[4] I. Daubechies, Ten Lectures on Wavelets, Society of Industrial and Applied Mathematics, Philadelphia, 1992.
[5] A.T. Degani, J.D.A. Walker, F.T. Simith, Unsteady separation past moving surfaces, J. Fluid Mech. 375 (1998) 1–38.
[6] D. Donoho, I. Johnstone, Ideal spatial adaptation via wavelet shrinkage, Biometrica 81 (1994) 425–455.
[7] M. Farge, Wavelet Transform and their Application to Turbulence, Ann. Rev. Fluid Mech. 24 (1992) 395–457.
[8] Wavelet Toolbox User's Guide, http://www.mathworks.com.
[9] G. Haller, Chaos Near Resonances, Springer, New York, 1999.
[10] G. Haller, Finding finite-time invariant manifolds in two-dimensional velocity data, Chaos 10 (2000) 99–108.
[11] G. Haller, Exact theory of unsteady separation for two-dimensional flows, J. Fluid Mech. 512 (2004) 257–311.
[12] A.L. Hodgkin, A.F. Huxley, A quantitative description of membrane current and its applications to conduction and excitation in nerve, J. Phys. 117 (1952) 500–544.
[13] C. Jones, Geometric Singular Perturbation Theory C. I. M. E. Lectures, in: Lecture Notes in Mathematics, vol. 1609, Springer, Heidelberg, 1995.
[14] G. Kaiser, A Friendly Guide to Wavelets, Birkhauser, 1994.
[15] M.S. Kilic, G. Haller, A. Nesihtadt, Unsteady flow separation by the method of averaging, Phys. Fluids (2005).
[16] S.G. Mallat, A Signal Processing Tour of Wavelets, Academic Press, San Diego, 1998.
[17] S. Mittal, B. Kumar, Flow past a rotating cylinder, J. Fluid Mech. 476 (2003) 303–334.
[18] A.S. Monin, A.M. Yaglom, Statistical fluid mechanics: Mechanics of Turbulence Volume 1, MIT Press, Cambridge, 1971.
[19] A.C. Newell, J.V. Moloney, Nonlinear Optics, Addison Wesley Publishing Co, 1992.
[20] J.C. Padrino, D.D. Joseph, Numerical Study of the Steady State Uniform Flow Past a Rotating Cylinder, 2004.
[21] L. Prandtl, Über Flüssigkeitsbewegung bei sehr kleiner Reibung, in: Verh. III, Int. Math. Kongr., Heidelberg, 1904, pp. 484–491.
[22] A.E. Perry, M.S. Chong, A series expansion study of the Navier–Stokes equations with applications to three-dimensional separation patterns, J. Fluid Mech. 173 (1986) 207–223.
[23] H. Schlichting, K. Gersten, Boundary-Layer Theory, Springer, New York, 2000.
[24] W.R. Sears, D.P. Tellionis, Boundary-layer separation in unsteady flow, SIAM J. Appl. Math. 28 (1975) 215–235.